The Astrophysical Journal, 775:127 (20pp), 2013 October 1 doi:10.1088/0004-637X/775/2/127

DIAGNOSTICS OF AGN-DRIVEN MOLECULAR OUTFLOWS IN ULIRGs FROM *HERSCHEL*-PACS OBSERVATIONS OF OH AT 119 μm

H. W. W. Spoon[1], D. Farrah[2], V. Lebouteiller[1,3], E. González-Alfonso[4], J. Bernard-Salas[5], T. Urrutia[6], D. Rigopoulou[7,8], M. S. Westmoquette[9], H. A. Smith[10], J. Afonso[11,12], C. Pearson[13,14], D. Cormier[15], A. Efstathiou[16], C. Borys[17], A. Verma[7], M. Etxaluze[18], and D. L. Clements[19]

[1] Cornell University, CRSR, Space Sciences Building, Ithaca, NY 14853, USA; spoon@isc.astro.cornell.edu
[2] Department of Physics, Virginia Tech, Blacksburg, VA 24061, USA
[3] CEA-Saclay, DSM/IRFU/SAp, F-91191 Gif-sur-Yvette, France
[4] Departamento de Física y Matemáticas, Universidad de Alcalá, Campus Universitario, E-28871 Alcalá de Henares, Madrid, Spain
[5] Department of Physical Sciences, Milton Keynes MK7 6AA, UK
[6] Leibniz Institut für Astrophysik, Potsdam, An der Sternwarte 16, D-14482 Potsdam, Germany
[7] Department of Physics, Denys Wilkinson Building, Keble Road, Oxford OX1 3RH, UK
[8] RAL Space, Science and Technology Facilities Council, Rutherford Appleton Laboratory, Didcot OX11 0QX, UK
[9] European Southern Observatory, Karl-Schwarzschild-Str. 2, D-85748 Garching bei München, Germany
[10] Harvard-Smithsonian Center for Astrophysics, 60 Garden Street, Cambridge, MA 02138, USA
[11] Centro de Astronomia e Astrofísica da Universidade de Lisboa, Observatório Astronómico de Lisboa, Tapada da Ajuda, 1349-018 Lisbon, Portugal
[12] Department of Physics, Faculty of Sciences, University of Lisbon, Campo Grande, 1749-016 Lisbon, Portugal
[13] RAL Space, Rutherford Appleton Laboratory, Harwell, Oxford OX11 0QX, UK
[14] Department of Physics and Astronomy, The Open University, Milton Keynes MK7 6AA, UK
[15] Institut für theoretische Astrophysik, Zentrum für Astronomie der Universität Heidelberg, Albert-Ueberle Str. 2, D-69120 Heidelberg, Germany
[16] School of Sciences, European University Cyprus, Diogenes Street, Engomi, 1516 Nicosia, Cyprus
[17] Infrared Processing and Analysis Center, California Institute of Technology, MS 100-22, Pasadena, CA 91125, USA
[18] Departamento de Astrofísica. Centro de Astrobiología. CSIC-INTA. Torrejón de Ardoz, E-28850 Madrid, Spain
[19] Physics Department, Imperial College London, Prince Consort Road, London SW7 2AZ, UK
Received 2013 April 15; accepted 2013 July 22; published 2013 September 16

ABSTRACT

We report on our observations of the 79 and 119 μm doublet transitions of OH for 24 local ($z < 0.262$) ULIRGs observed with *Herschel*-PACS as part of the Herschel ULIRG Survey (HERUS). Some OH 119 μm profiles display a clear P-Cygni shape and therefore imply outflowing OH gas, while other profiles are predominantly in absorption or are completely in emission. We find that the relative strength of the OH emission component decreases as the silicate absorption increases. This result locates the OH outflows inside the obscured nuclei. The maximum outflow velocities for our sources range from less than 100 to ~2000 km s^{-1}, with 15/24 (10/24) sources showing OH absorption at velocities exceeding 700 km s^{-1} (1000 km s^{-1}). Three sources show maximum OH outflow velocities exceeding that of Mrk231. Since outflow velocities above 500–700 km s^{-1} are thought to require an active galactic nucleus (AGN) to drive them, about two-thirds of our ULIRG sample may host AGN-driven molecular outflows. This finding is supported by the correlation we find between the maximum OH outflow velocity and the IR-derived bolometric AGN luminosity. No such correlation is found with the IR-derived star formation rate. The highest outflow velocities are found among sources that are still deeply embedded. We speculate that the molecular outflows in these sources may be in an early phase of disrupting the nuclear dust veil before these sources evolve into less-obscured AGNs. Four of our sources show high-velocity wings in their [C II] fine-structure line profiles, implying neutral gas outflow masses of at least (2–4.5) $\times$ 10^8 $M_\odot$.

Key words: infrared: galaxies – ISM: jets and outflows – galaxies: evolution – galaxies: ISM – quasars: absorption lines

Online-only material: color figures

1. INTRODUCTION

The degree to which active galactic nuclei (AGNs) affect their kiloparsec to megaparsec scale surroundings is a key idea in understanding the cosmological assembly history of galaxies. This idea, commonly termed "AGN feedback," can take several forms; we focus here on the specific case where a central supermassive black hole exerts a strong influence on short (~10^7 yr) timescales and ~kpc spatial scales to quench star formation in its host galaxy. Such feedback is thought to occur when radiation from the accretion disk drives a wind of partially ionized gas into the host, which then empties the galaxy of fuel for star formation by kinetically driving the interstellar medium (ISM) gas out of the galaxy and/or heating the ISM so it cannot collapse to form stars. Feedback is thought to be particularly effective in galaxy mergers, after the progenitor nuclei have coalesced (Di Matteo et al. 2005; Debuhr et al. 2012; Choi et al. 2012). IR-luminous galaxy mergers, which often harbor both high rates of star formation and luminous AGNs, are thus prime sites to study the properties and effects of AGN feedback.

There is a strong theoretical motivation for AGN feedback from models that trace the assembly of galaxies with redshift. Models without quasar mode feedback have great difficulty reproducing the observed redshift evolution of the galaxy mass function (Somerville et al. 2001; Benson et al. 2003), whereas models with a prescription for AGN feedback show dramatic improvements in their consistency with observations (Croton et al. 2006; Somerville et al. 2008). Moreover, simulations of individual galaxies suggest that quasar mode feedback has a profound influence (e.g., Hopkins & Elvis 2010). Observational

diagnostics of AGN feedback are, however, relatively sparse. AGN feedback has been inferred indirectly from, e.g., the discovery of winds with high kinetic fluxes in ULIRGs and QSOs (Moe et al. 2009; Rupke & Veilleux 2011) and directly from e.g., the star formation properties of QSO host galaxies (Farrah et al. 2012). However, some recent claims for quasar-driven suppression of star formation (Page et al. 2012) are controversial (Harrison et al. 2012).

A promising avenue for diagnosing the properties of AGN-driven outflows, with the eventual aim of understanding the feedback phenomenon, is to examine outflows of *molecular* gas. In ULIRGs, such outflows may be expected to trace the earliest stages of AGN feedback activity, when the AGN itself is still obscured. These outflows also provide the only direct evidence that the fuel for star formation is being removed. Moreover, molecular outflows have been observed previously in IR-luminous galaxy mergers (Sturm et al. 2011; Chung et al. 2011; Fischer et al. 2010; Sakamoto et al. 2009; Walter et al. 2002; Baan et al. 1989). The observational study of such outflows is however still in its infancy; we currently lack even a broad phenomenological picture of how and when outflow activity is seen in molecular lines and what other properties of the merger the molecular line profiles show relationships with.

The Herschel ULIRG Survey (HERUS) is well situated to examine the range of properties of an important molecular tracer, hydroxyl (OH), in local IR-luminous mergers. HERUS has obtained spectroscopic observations of two ground-state doublets of OH, at 79 μm and 119 μm, in 24 local ULIRGs. In this paper, we present a summary of the full OH data set, analyze the velocity profiles, and compare them to line profiles of mid- and far-IR fine-structure lines. Modeling of the sources will be presented in subsequent HERUS papers. In Section 2, we review observations of OH in the literature. In Section 3, we present new observations we obtained using *Herschel*. In Section 4, we analyze the velocity profiles of the OH profiles and compare them to line profiles of mid- and far-IR fine-structure lines. In Section 5, we discuss and summarize our results. Throughout this paper, we assume $H_0 = 67.3$ km s^{-1} Mpc^{-1}, $\Omega_M = 0.315$, and $\Omega_\Lambda = 0.685$ (Planck Collaboration 2013).

2. BACKGROUND: OBSERVATIONS AND PROPERTIES OF OH

The first far-infrared detections of OH in the ISM were made by Storey et al. (1981) using the Kuiper Airborne Observatory: they measured the two 119 μm Λ-doubled lines between the ground and first excited states, which they discovered in absorption from Sgr B2 and in emission from the shock in Orion KL. This line is the strongest OH line, being from a ground-state absorption, but there are altogether 14 far-infrared lines between 34 μm and 163 μm, arising among the lowest eight rotational levels of OH. The transitions, which arise from levels lying 120 to 618 K above ground, are strong. The dipole moment for OH is large, 1.668 Debye (for comparison, the CO dipole moment is 0.112 Debye), so that the radiative rates for OH transitions are generally fast (for example, the Einstein A coefficient for the 119 μm doublet lines is about 0.136 s^{-1}, as compared to 7.2×10^{-8} s^{-1} for CO $J = 1$–0). Critical densities for OH are high (of the order 10^9 cm^{-3}), making these transitions sensitive to radiative pumping. The far-IR (FIR) OH transitions also include cross-ladder lines whose radiative rates are 100 times weaker, providing a data set of neighboring, far-IR lines that frequently includes both optically thin and very optically thick features. The OH analyses have an additional resource from which to draw: the strong hyper-fine radio wavelength transitions OH has in its ground state (1665 and 1667 MHz; 18cm), which have been extensively observed (e.g., Baan 1985; Baan et al. 1989; Henkel & Wilson 1990).

The *Infrared Space Observatory* (*ISO*) detected the remaining OH infrared lines from Galactic and/or extragalactic sources. Sylvester et al. (1997) used these lines to conclusively show that the 18 cm radio maser emission in evolved stars is pumped by absorption of the 34 μm dust continuum, while Skinner et al. (1997) proved the effectiveness of the IR pumping of megamasers in ULIRGs in the case of Arp 220. The *ISO* analyses and modeling of the OH line soon discovered their power and complexity, especially in conjunction with modeling the FIR fine-structure lines. Fischer et al. (1999), Bradford et al. (1999, NGC 253), Kegel et al. (1999, IRAS 20100−4156 and 3Zw35), González-Alfonso et al. (2004, Arp 220), Smith et al. (2004), Spinoglio et al. (2005, NGC 1068), and González-Alfonso et al. (2008, Mrk 231) found the OH lines either mostly in absorption (Arp 220; IRAS 20100−4156), mostly in emission (NGC 1068), or with a mix (Mrk 231; NGC 253). The models, which had to fit the dust continua and atomic fine-structure lines, usually required a small, warm nuclear region, a cooler extended region, and sometimes a third component as well, with evidence for collisional excitation, radiative pumping from the presence of warm dust continuum photons, and also signs of X-ray-dominated region excitation (later suggested for pumping the CO infrared lines as well). *Herschel* observations have dramatically improved the data set, not only in terms of sensitivity, but also because these observations resolved the line shapes in many cases. Fischer et al. (2010) reported the remarkable discovery that some of the OH lines show P-Cygni profiles, suggesting massive outflows, and Sturm et al. (2011) and González-Alfonso et al. (2010, 2012, 2013), among others, have begun to exploit and model the implications of these data. Outflows are expected to play a pivotal role in the evolutionary history of galaxies, and indeed radio observations of CO and HCN (Aalto et al. 2012; Feruglio et al. 2010) are now making inroads into this topic. It appears that the OH molecule plays a remarkable diagnostic role in that the combination of operative excitation mechanisms and optical depths for its many infrared lines allow it to be a much broader sensor of the various conditions in galaxies (nuclear regions, star formation complexes, outflows, etc.) than, for example, is CO, yet OH can have an abundance not much smaller than that of CO.

3. OBSERVATIONS

The HERUS (Farrah et al. 2013) is a far-IR photometric and spectroscopic atlas of the low-redshift ($z < 0.262$) ULIRG population with *Herschel*, and at 250 hr, was the largest extragalactic program in the Herschel Open Time 1 call. The sample comprises all 40 ULIRGs from the *IRAS*-PSCz (Saunders et al. 2000) with *IRAS* 60 μm flux densities $\geqslant$2 Jy, plus IRAS 00397−1312 (1.8 Jy), IRAS 07598+6508 (1.7 Jy), and IRAS 13451+1232 (1.9 Jy). All objects have been observed with the Infrared Spectrograph (IRS) onboard *Spitzer*. HERUS obtained SPIRE-FTS spectra for 29/43 sources and SPIRE photometry for 32/43 sources. PACS spectroscopy was obtained for any target not part of the 19 ULIRGs included in the SHINING program (Fischer et al. 2010; Sturm et al. 2011). The HERUS PACS subsample hence comprises 24 sources, whose observation details are shown in Table 1. Among these sources is the blazar 3C273, a ULIRG by luminosity, but otherwise not a late-stage merger. This source will hence not be considered

Table 1
PACS Observations Log

Galaxy	Line	ObsID	Obs Date	Spaxel Used[a]
00188−0856	OH119 and OH79	1342237570	2012 Jan 16	(3, 3)
00397−1312	OH79	1342238351	2012 Jan 25	(3, 3)
00397−1312	OH119	1342238350	2012 Jan 25	(3, 3)
01003−2238	OH119 and OH79	1342238371	2012 Jan 28	(3, 3)
Mrk1014	OH119 and OH79	1342238723	2012 Feb 6	(3, 3)
03158+4227	OH119 and OH79	1342238963	2012 Feb 11	(3, 3)
03521+0028	OH119 and OH79	1342239746	2012 Feb 26	(3, 3)
06035−7102	OH119 and OH79	1342239479	2012 Feb 15	(3, 3)
06206−6315	OH119 and OH79	1342230961	2011 Oct 14	(3, 3)
07598+6508	OH79[b]	1342243534	2012 Mar 25	(3, 3)
07598+6508	OH119[c]	1342231959	2011 Nov 6	(3, 3)
08311−2459	OH119 and OH79	1342230967	2011 Oct 14	(3, 3)
10378+1109	OH119 and OH79	1342232315	2011 Nov 14	(3, 3)
11095−0238	OH119 and OH79	1342232612	2011 Nov 22	(3, 3)
12071−0444	OH119 and OH79	1342234994	2011 Dec 20	(3, 3)
3C273	OH119 and OH79	1342235707	2011 Dec 29	(3, 3)
13451+1232	OH119 and OH79	1342236886	2012 Jan 9	(3, 3)
Mrk463	OH119 and OH79	1342236982	2012 Jan 8	(3, 3)
15462−0450	OH119 and OH79	1342238135	2012 Jan 22	(3, 3)
16090−0139	OH119 and OH79	1342238907	2012 Feb 10	(3, 3)
19254−7245	OH119 and OH79	1342231722	2011 Oct 31	(2, 2)+(2, 3)+(3, 3)
20087−0308	OH119 and OH79	1342232302	2011 Nov 13	(3, 3)
20100−4156	OH119 and OH79	1342216371	2011 Mar 18	(3, 3)
20414−1651	OH119 and OH79	1342217908	2011 Apr 3	(3, 3)
23230−6926	OH119 and OH79	1342234997	2011 Dec 21	(3, 3)
23253−5415	OH119 and OH79	1342235703	2011 Dec 28	(3, 3)

Notes.
[a] Spaxel (3, 3) is the central spaxel in the 5 × 5 footprint.
[b] Observed as part of program `OT1_dweedman_1`. The HERUS observation was mispointed.
[c] Observed as part of program `OT1_sveilleu_3`. The HERUS observation was mispointed.

in Section 4.5 and beyond, where we discuss the evolutionary aspects of dusty mergers.

The PACS spectroscopy observations for the HERUS program were performed between 2011 March 18 and 2012 April 8 (OD673–OD1060). The PACS integral-field spectrometer samples the spatial direction with 25 pixels and the spectral direction with 16 pixels. Each spectral pixel "sees" a distinct wavelength range that is scanned by varying the grating angle, and the combination of the 16 ranges makes the total spectrum. The 5 × 5 spatial pixels ("spaxels") constitute a field of view of 47″ × 47″, much larger than the far-IR source sizes. The coordinates were chosen to center the object in the central spaxel. According to the PACS Observer's Manual,[20] the point-spread function FWHM is ≈9.″5 between 55 and 100 μm, and it increases to about ≈14″ at 200 μm (the longest observed wavelength in our sample is 199 μm).

Observations were performed in range spectroscopy mode with a spectral range somewhat larger than that used for line spectroscopy mode. For a given feature, the width of the spectral range was chosen to accommodate possible uncertainties in the redshift, as well as accounting for blue wings and blueshifts and for intrinsic line broadening. The chop/nod observation mode was used, in which the source was observed by alternating between the on-source position and a clean off-source position. The smallest throw (±1.′5) was used to reduce the effect of field rotation between the two chop positions. Two nod positions were used in order to completely eliminate the telescope background emission.

[20] http://herschel.esac.esa.int/Docs/PACS/html/pacs_om.html

We observed all the HERUS objects in the following lines: 52 μm [O III], 57 μm [N III], 63 μm [O I], 145 μm [O I], and 158 μm [C II]. In addition, the 122 μm [N II] line was observed together with the 119 μm OH doublet (OH119). Since the PACS spectrometer observes simultaneously in two bands, the 79 μm OH doublet (OH79) was observed in the blue band while 158 μm [C II] was observed in the red band. Results for our fine-structure line observations are presented in Farrah et al. (2013).

The data reduction was performed in HIPE `8.0` (Ott 2010) using the default chop/nod pipeline script. The level 1 product (calibrated in flux and in wavelength, with bad pixels masks according to the HIPE reduction criteria) was then exported and processed by our in-house PACSman tool (Lebouteiller et al. 2012) for further data flagging, spectral rebinning, and empirical error estimates.

In this paper, we focus on the spectra of the brightest spaxel in the field—typically spaxel (3, 3)—and perform a point source flux correction. There are, however, exceptions. For IRAS 19254−7245 ("the Super Antennae") we intended to point to its southern nucleus. An error on the input coordinates meant that this nucleus fell between spaxels (2, 2), (2, 3), and (3, 3). Since all three spaxels show an equal continuum brightness, we co-added their spectra; see Table 1.

Also, for two other sources in our sample inaccurate coordinates were used to obtain our spectra. IRAS 03158+4227 was mispointed by about half a spaxel and IRAS 07598+6508 was mispointed by about two spaxels, thereby placing the source at an edge spaxel. For the latter source, we therefore substituted

Table 2
Basic Observational Quantities for the HERUS Sample

Galaxy	Redshift[a]	$\log L_{IR}$[b]$/L_\odot$	f_{30}/f_{15}[c]	α[d]	$\log L_{AGN,bol}$[e]$/L_\odot$	SFR[f] ($M_\odot$ yr^{-1})	S_{sil}[g]	EQW62[h] (μm)
00188−0856	0.1287	12.39	9.05	0.51	$12.16^{+0.11}_{-0.15}$	119^{+36}_{-36}	−2.6	0.066
00397−1312	0.2617	12.90	6.29	0.67	$12.79^{+0.09}_{-0.11}$	263^{+119}_{-119}	−2.9	0.026
01003−2238	0.1179	12.32	3.88	0.83	$12.30^{+0.07}_{-0.09}$	36^{+31}_{-31}	−0.8	0.040
Mrk 1014	0.1631	12.62	5.65	0.71	$12.53^{+0.08}_{-0.10}$	121^{+62}_{-62}	0.2	0.080
03158+4227	0.1346	12.63	9.93	0.47	$12.36^{+0.12}_{-0.17}$	227^{+63}_{-63}	−3.1	0.059
03521+0028	0.1519	12.52	20.21	0.06	$11.39^{+0.52}_{-2.00}$	309^{+21}_{-49}	−1.3	0.356
06035−7102	0.0795	12.22	7.50	0.60	$12.06^{+0.10}_{-0.13}$	66^{+24}_{-24}	−1.5	0.087
06206−6315	0.0921	12.23	10.72	0.43	$11.92^{+0.13}_{-0.19}$	96^{+25}_{-25}	−1.6	0.183
07598+6508	0.1487	12.50	2.74	0.91	$12.52^{+0.04}_{-0.08}$	28^{+47}_{-28}	0.1	0.006
08311−2459	0.1005	12.50	4.36	0.79	$12.46^{+0.08}_{-0.09}$	65^{+47}_{-47}	−0.5	0.139
10378+1109	0.1363	12.31	13.55	0.30	$11.85^{+0.17}_{-0.30}$	142^{+30}_{-30}	−2.1	0.091
11095−0238	0.1063	12.28	9.56	0.49	$12.03^{+0.12}_{-0.16}$	97^{+28}_{-28}	−3.3	0.037
12071−0444	0.1289	12.41	4.95	0.75	$12.35^{+0.08}_{-0.10}$	63^{+38}_{-38}	−1.4	0.087
3C273	0.1586	12.80	1.38	1.00	$12.86^{+0.00}_{-0.07}$	<94	0.1	<0.007
Mrk 231[i]	0.0422	12.55	4.10	0.81	$12.52^{+0.07}_{-0.09}$	67^{+53}_{-53}	−0.7	0.010
13451+1232	0.1218	12.32	4.01	0.82	$12.29^{+0.07}_{-0.09}$	38^{+31}_{-31}	−0.3	<0.022
Mrk 463	0.0508	11.79	1.89	0.98	$11.84^{+0.01}_{-0.07}$	1^{+9}_{-1}	−0.4	<0.005
15462−0450	0.1003	12.24	6.94	0.63	$12.10^{+0.09}_{-0.12}$	64^{+26}_{-26}	−0.4	0.062
16090−0139	0.1336	12.55	10.63	0.43	$12.25^{+0.13}_{-0.18}$	200^{+53}_{-53}	−2.5	0.071
19254−7245	0.0619	12.09	5.17	0.74	$12.02^{+0.08}_{-0.10}$	32^{+18}_{-18}	−1.3	0.066
20087−0308	0.1057	12.42	16.07	0.20	$11.79^{+0.24}_{-0.57}$	209^{+39}_{-39}	−1.8	0.367
20100−4156	0.1296	12.67	14.45	0.27	$12.16^{+0.19}_{-0.36}$	343^{+70}_{-70}	−2.7	0.089
20414−1651	0.0869	12.22	22.86	0.00[j]	<11.46	165^{+0}_{-24}	−1.6	0.570
23230−6926	0.1064	12.37	13.25	0.32	$11.93^{+0.17}_{-0.28}$	160^{+35}_{-35}	−2.1	0.324
23253−5415	0.1298	12.36	15.36	0.23	$11.78^{+0.22}_{-0.46}$	176^{+34}_{-34}	−1.5	0.235

Notes.
[a] Determined from far-IR fine-structure lines.
[b] $L_{IR} = L(8–1000\,\mu m)$ integrated from spectral energy distributions consisting of *Spitzer*-IRS spectra, *IRAS*, *ISO*-PHT photometry, and *Herschel*-SPIRE photometry.
[c] Ratio of 30–15 μm continuum.
[d] Fraction of L_{bol} contributed by the AGN, α, derived using method 6 of Veilleux et al. (2009). We assume the uncertainty on α to be ± 0.15.
[e] Derived using method 6 by Veilleux et al. (2009). This method uses f_{30}/f_{15} to infer α.
[f] Using SFR $= (1-\alpha) \times 10^{-10}\ L_{IR}$, as adopted by Sturm et al. (2011).
[g] Silicate strength (Spoon et al. 2007): >0 for silicate emission features, <0 for silicate absorption features.
[h] Ice-corrected equivalent width of the 6.2 μm PAH feature (Spoon et al. 2007).
[i] Observed as part of the SHINING sample (Fischer et al. 2010).
[j] Methods 3–6 of Veilleux et al. (2009) estimate $\alpha = 0$. Only method 2, based on the detection of 14.32 μm [Ne v] (Farrah et al. 2007), estimates $\alpha = 0.60$.

the HERUS observations of OH79 and OH119 for those obtained by Sargsyan et al. (2012; program `OT1_dweedman_1`) and Veilleux et al. (program `OT1_sveilleu_3`), respectively.

The redshifts for our sources were obtained from observations of 158 μm [C II], 122 μm [N II], and 63 μm [O I], and have been tabulated in Table 2.

4. ANALYSIS

Our spectra of the 119 μm ^{16}OH (OH119) and 120 μm ^{18}OH (^{18}OH120) doublets are shown in Figure 1. Each spectrum covers a velocity range of −2500 to +5000 km s^{-1} with respect to the bluest of the two OH119 doublet components (λ_{rest} = 119.233 μm; $\Delta v_{doublet}$ = 520 km s^{-1}). The redshifts used to define the systemic velocity (v_{sys}) for this line are given in Table 2. Apart from OH119 and ^{18}OH120, several other species have lines in this range: CH^+ (at v = +1546 km s^{-1}) and CH at −1330 and −2080 km s^{-1}. The latter species is not detected in any of our sources. Here, we will assume that a clean continuum

Table 3
OH Line Log

Line	λ[a] (μm)
^{18}OH $\Pi_{1/2} - \Pi_{3/2}$ $\frac{1^-}{2} - \frac{3^+}{2}$	79.083
^{16}OH $\Pi_{1/2} - \Pi_{3/2}$ $\frac{1^-}{2} - \frac{3^+}{2}$	79.118
^{18}OH $\Pi_{1/2} - \Pi_{3/2}$ $\frac{1^+}{2} - \frac{3^-}{2}$	79.147
^{16}OH $\Pi_{1/2} - \Pi_{3/2}$ $\frac{1^+}{2} - \frac{3^-}{2}$	79.181
^{16}OH $\Pi_{3/2} - \Pi_{3/2}$ $\frac{5^-}{2} - \frac{3^+}{2}$	119.233
^{16}OH $\Pi_{3/2} - \Pi_{3/2}$ $\frac{5^+}{2} - \frac{3^-}{2}$	119.441
^{18}OH $\Pi_{3/2} - \Pi_{3/2}$ $\frac{5^-}{2} - \frac{3^+}{2}$	119.964
^{18}OH $\Pi_{3/2} - \Pi_{3/2}$ $\frac{5^+}{2} - \frac{3^-}{2}$	120.171

Note. [a] The tabulated rest wavelengths are averages of the rest wavelengths of the two blended hyper-fine lines.

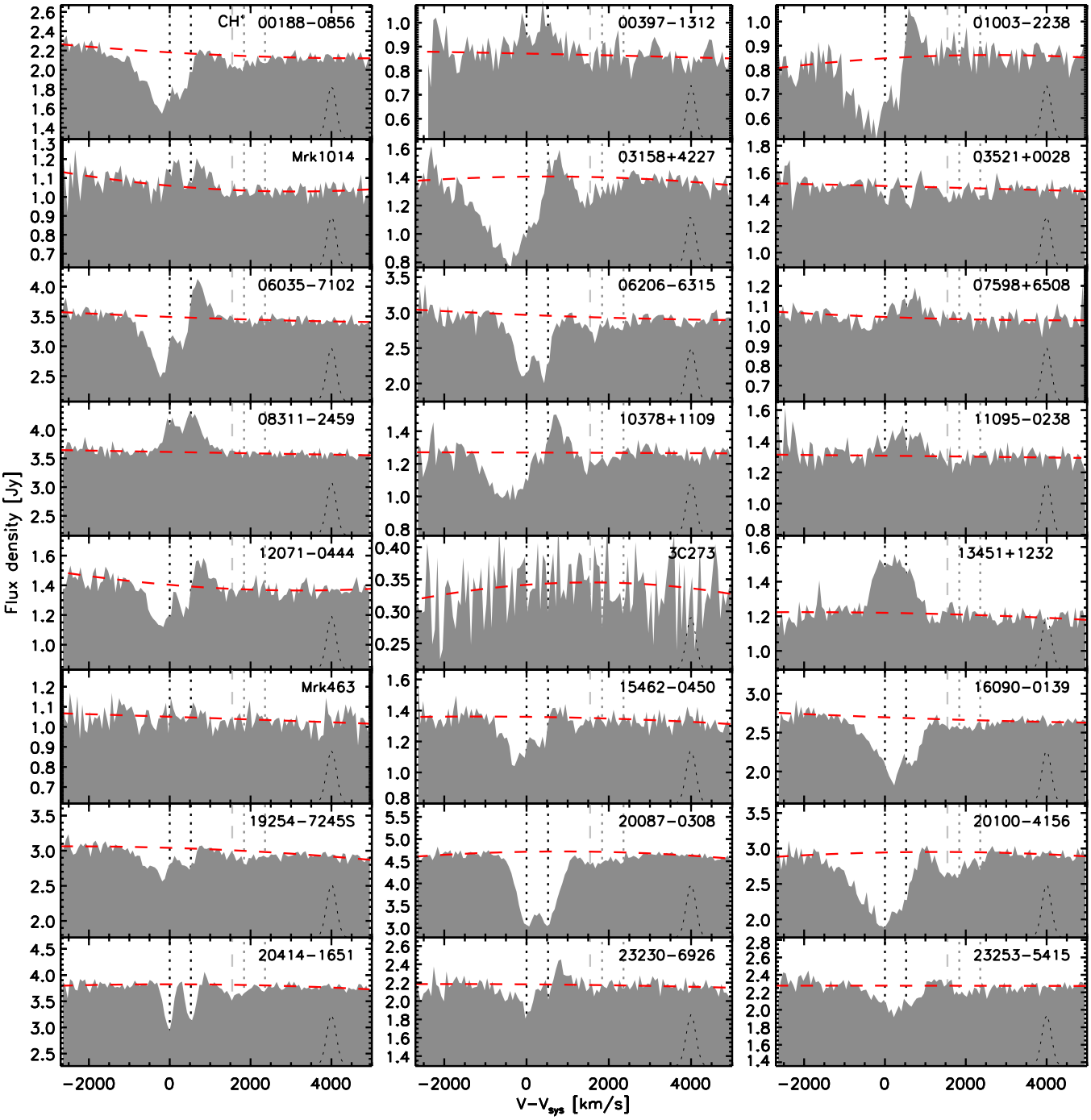

Figure 1. *Herschel*-PACS spectra of the partially blended 119 μm ^{16}OH and ^{18}OH doublets for ULIRGs observed in the HERUS survey. All spectra have the same flux dynamic range. The systemic velocity is defined as the rest wavelength of the ^{16}OH $\Pi_{3/2}$–$\Pi_{3/2}$ $(5^-/2)$ – $(3^+/2)$ transition at 119.233 μm. The rest velocities of the ^{16}OH and ^{18}OH lines (see Table 3) are indicated by black and gray dotted vertical lines, respectively. Potential contamination by CH^+ (119.848 μm) is indicated by a light gray dashed vertical line at $v = +1543$ km s^{-1}. The adopted local continuum is shown in red. The spectral resolution is shown by a dashed black Gaussian profile in the bottom right corner of each panel.

(A color version of this figure is available in the online journal.)

exists at $v < -2000$ km s^{-1} and at $v > +2500$ km s^{-1}. The local continuum resulting from a second order polynomial interpolation between these two continuum ranges is shown as a dashed red line in Figure 1.

The corresponding spectra of the OH79 and ^{18}OH79 doublets, where the latter refers to the 79 μm ^{18}OH feature, are shown in Figure 3. The spectra cover a velocity range of −2500 to +2000 km s^{-1} with respect to the bluest of the two OH79 doublet components ($\lambda_{\rm rest} = 79.118$ μm; $\Delta v_{\rm doublet} = 240$ km s^{-1}) and have been rebinned to channels of ∼80 km s^{-1} velocity width to make up for the poor signal to noise ratio (S/N). Unlike the OH119 and ^{18}OH120 doublets, which are separated by ∼1900 km s^{-1}, the two 79 μm OH isotope doublets are strongly blended at the resolution of the instrument. Apart

from these OH doublets, the spectral range also includes the 78.742 μm H_2O 4_{23}–3_{12} transition (at $v = -1425$ km s^{-1}), which may be detected in several of our sources (most clearly in IRAS 20087−0308, 20100−4156, and 23230−6923). Given the poor S/N of the OH79 spectra, the continuum was fit using first order polynomials only.

4.1. Examination of the OH119 Profiles

The spectra in Figure 1 show a great variety of OH119 profiles, ranging from pure absorption profiles (e.g., IRAS 06206−6315 and 20087−0308), to P-Cygni profiles (e.g., IRAS 06035−7102 and 12071−0444), to pure emission profiles (e.g., IRAS 00397−1312 and 13451+1232). The normalized versions of these spectra, shown in Figure 2, further reveal that the contrast and equivalent width of the OH119 features vary greatly. The deepest absorption feature is seen in IRAS 03158+4227 and the strongest emission feature in IRAS 13451+1232. The relative strength of the ^{18}OH120 to the OH119 doublets also appears to vary within the sample. ^{18}OH120 seems absent in IRAS 08311−2459 and very strong in IRAS 20100−4156.

The double peaked nature of the OH119 doublet is evident in most spectra, although there are some sources, such as IRAS 10378+1109 and 13451+1232, where it is not self-evident. Perhaps this signature is washed out in these sources due to a strong velocity gradient or the existence of several velocity components. In our sample, the velocity range over which the OH absorption and/or emission occurs varies greatly. The narrowest velocity range is found in IRAS 20414−1651, where both OH119 doublet lines appear to be unresolved. The widest velocity field likely occurs in IRAS 03158+4227. Note that in the latter source, the lowest blueshifted outflow velocity amounts to ∼400 km s^{-1}, whereas in IRAS 20100−4156, for example, quiescent gas (gas at $v \approx 0$) also appears to be present. In Mrk 1014, the entire OH119 profile, seen in emission, seems to be redshifted by 200–300 km s^{-1}. Some of our sources furthermore show a lack of redshifted emitting high-velocity gas at similar velocities as the blueshifted absorbing gas. The clearest example may be the OH119 profile of IRAS 01003−2238, since this OH119 profile is not contaminated by ^{18}OH120 emission or absorption. The significance of this disparity will be discussed in Section 4.3.

Due to the relatively small separation in velocity space between the four OH and ^{18}OH lines (∼500 km s^{-1} between doublet lines and ∼2000 km s^{-1} between ^{16}OH and ^{18}OH isotopes), it is generally not straightforward to extract basic kinematic information from the blended profiles without involving model fits. If, for instance, OH and ^{18}OH exist out to velocities more blueshifted than −1000 km s^{-1} and more redshifted than +1000 km s^{-1}, the ^{18}OH120 complex will bleed into the OH119 complex. Hence, only within 500 km s^{-1} of the highest blueshifted velocity of the 119.233 μm OH line and within 500 km s^{-1} of the highest redshifted velocity of the 120.171 μm ^{18}OH line can one be certain that the other doublet line and the other isotope do not contribute to the spectral structure. We will use this fact in Section 4.4 to determine the highest velocity blueshifted OH gas.

4.2. Examination of the OH79 Profiles

Our sample of OH79 spectra (shown in Figure 3) generally has lower S/N than the corresponding sample of OH119 spectra, even after rebinning to channels of 80 km s^{-1}. Combined with a lower feature contrast (typically <10% of the continuum; Sturm et al. 2011, compared to up to 45% for OH119), this result makes examination of individual profiles more challenging for OH79 that for OH119.

Our sample of OH79 profiles lacks the deep blueshifted OH absorption components that are present in many of our OH119 profiles. Instead, the most clearly detected feature in the OH79 spectra (in about 50% of the sample) is a redshifted OH emission component. These emission components range from pure emission profiles (IRAS 08311−2459, 11095−0238, and 13451+1232), to redshifted P-Cygni components (IRAS 01003−2238, 03158+4227, 06035−7102, 10378+1109, 12071−0444, 15462−0450, 20100−4156), to pure absorption profiles (IRAS 20087−0308). The majority of our OH79 profiles are hard to classify.

The differences between the overall appearance of the OH119 and OH79 profile samples may seem surprising, given that both doublet complexes are the result of transitions between the $\Pi_{3/2}$ ground-state level and the lowest excited level in the $\Pi_{1/2}$ and $\Pi_{3/2}$ ladders. There are, however, important differences between these transitions. The Einstein B coefficients of the OH79 transitions are about 40 times lower than those of the OH119 transitions (Fischer et al. 2010), implying higher optical depths in the OH119 doublet than in the OH79 doublet. The latter doublet is therefore far better suited to measuring the OH column density than the optically thick OH119 doublet, but it also requires far higher S/N to detect the column density.

There are, however, conditions under which it is not straightforward to measure the OH column density from the OH79 doublet and these conditions depend on which of the pathways available to radiatively pump the molecule dominates. Unlike the OH119 doublet, which is an in-ladder ground-state transition in the $\Pi_{3/2}$ ladder, the OH79 doublet is a cross-ladder transition between the $\Pi_{3/2}$ and $\Pi_{1/2}$ ladders. This distinction is important as there are two other cross-ladder ground-state transitions that can very effectively pump the $\Pi_{1/2}$ levels above the OH79 upper level by absorbing 35 μm or 53 μm IR dust continuum photons (see, e.g., Spinoglio et al. 2005; González-Alfonso et al. 2012). A similar ground-state pumping mechanism for levels above the OH119 upper level does not exist in the $\Pi_{3/2}$ ladder. As there are no strong[21] (or efficient) cross-ladder transitions from the $\Pi_{1/2}$ ladder to the $\Pi_{3/2}$ OH119 upper level, most radiative cascades from the $\Pi_{1/2}$ ladder to the ground state (in the $\Pi_{3/2}$ ladder) take place through the OH79 transition. So, while the OH119 upper level is almost exclusively excited through the absorption of a 119 μm photon,[22] the OH79 upper level may become populated not only by the absorption of 79 μm photons but also by the absorption of 35 and 53 μm IR dust continuum photons. This situation opens the possibility for OH79 to be purely in emission while OH119 shows an absorption component. In our sample, we cannot identify a single case in which the nature of the OH79 profile differs from that of the OH119 profile. That is, as far as the S/N of our spectra permits, none of the sources for which OH119 shows an absorption component show OH79 purely in emission, or vice versa.

Further direct comparisons between the OH79 and OH119 profiles are complicated by the different doublet spacings

[21] The Einstein A coefficient for a cascade from the $\Pi_{1/2}$ $J = 3/2$ level to the $\Pi_{1/2}$ $J = 1/2$ level (163 μm OH doublet) is seven times larger than for a cross-ladder cascade to the OH119 upper level in the $\Pi_{3/2}$ ladder (96 μm OH doublet).

[22] Collisional excitation in a dense/warm environment is of course also a viable way to populate the OH119 upper level.

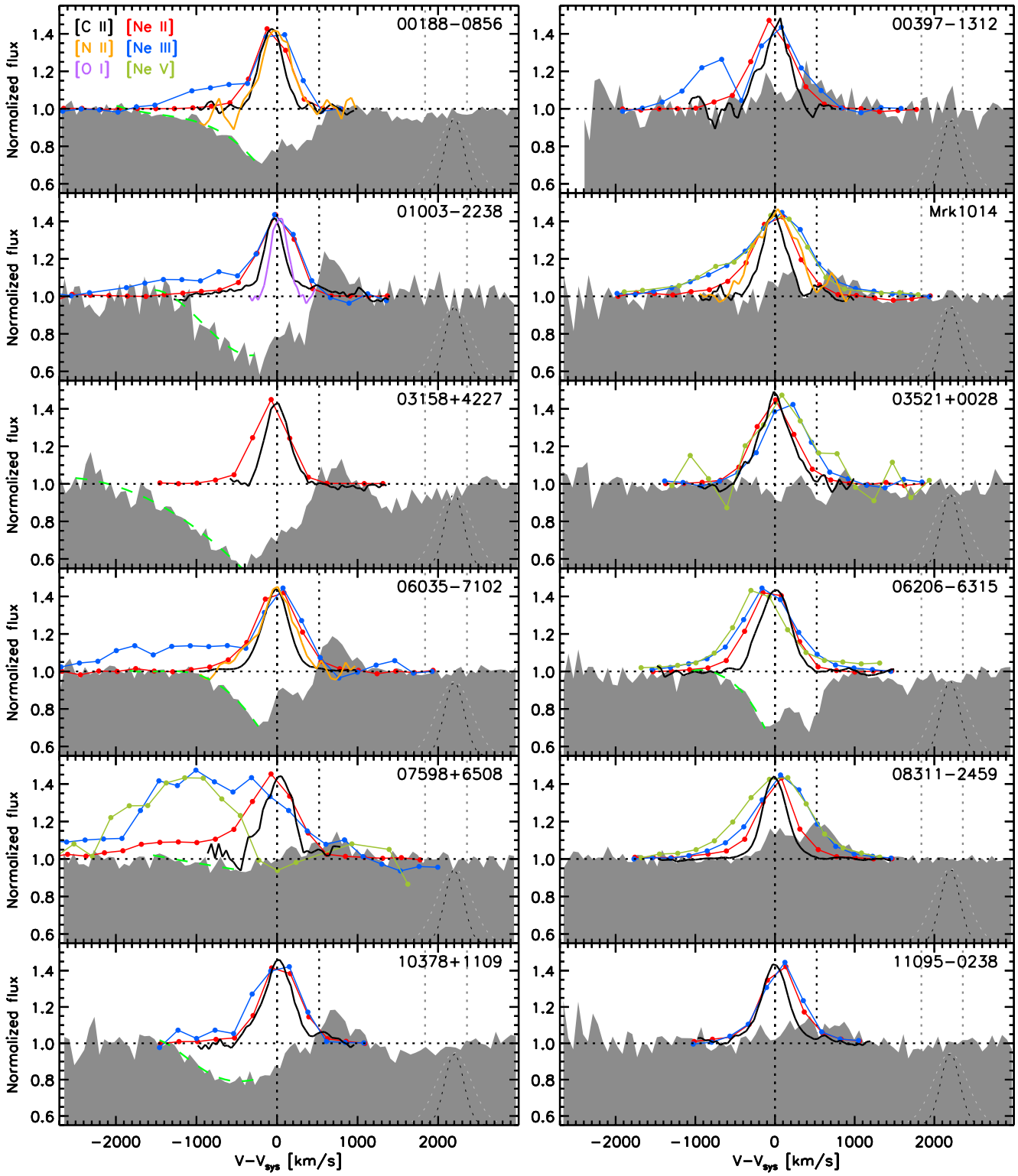

Figure 2. Comparison of the normalized 119 μm OH doublet profile to the scaled, smoothed emission line profiles of mid- and far-IR fine-structure lines. The rest velocities of the ^{16}OH and ^{18}OH lines (see Table 3) are indicated by black and gray dotted lines, respectively. Line profiles of 12.81 μm [Ne II], 15.56 μm [Ne III], and 14.32 μm [Ne V] are color-coded as red, blue, and green dotted lines, respectively. [C II] is shown in black, 122 μm [N II] is shown in orange, and 63 μm [O I] is shown in purple. The B-spline fit to the blue wing of the OH119 profile is shown as a green dashed curve. The spectral resolution of the OH119 line is shown by a dashed black Gaussian profile in the bottom right corner of each panel. The *Spitzer*-IRS-SH spectral resolution is shown as a light gray profile.

(A color version of this figure is available in the online journal.)

and the different isotope spacings for these OH complexes. For instance, the red emission component of an OH79 P-Cygni profile always appears closer to systemic velocity (by 300 to 500 km s^{-1}; e.g., IRAS 01003−2238, 06035−7102, and 10378+1109) than the red emission component of the corresponding OH119 doublet. This substantial difference can be partially explained by the differences in doublet spacings between OH79 and OH119.

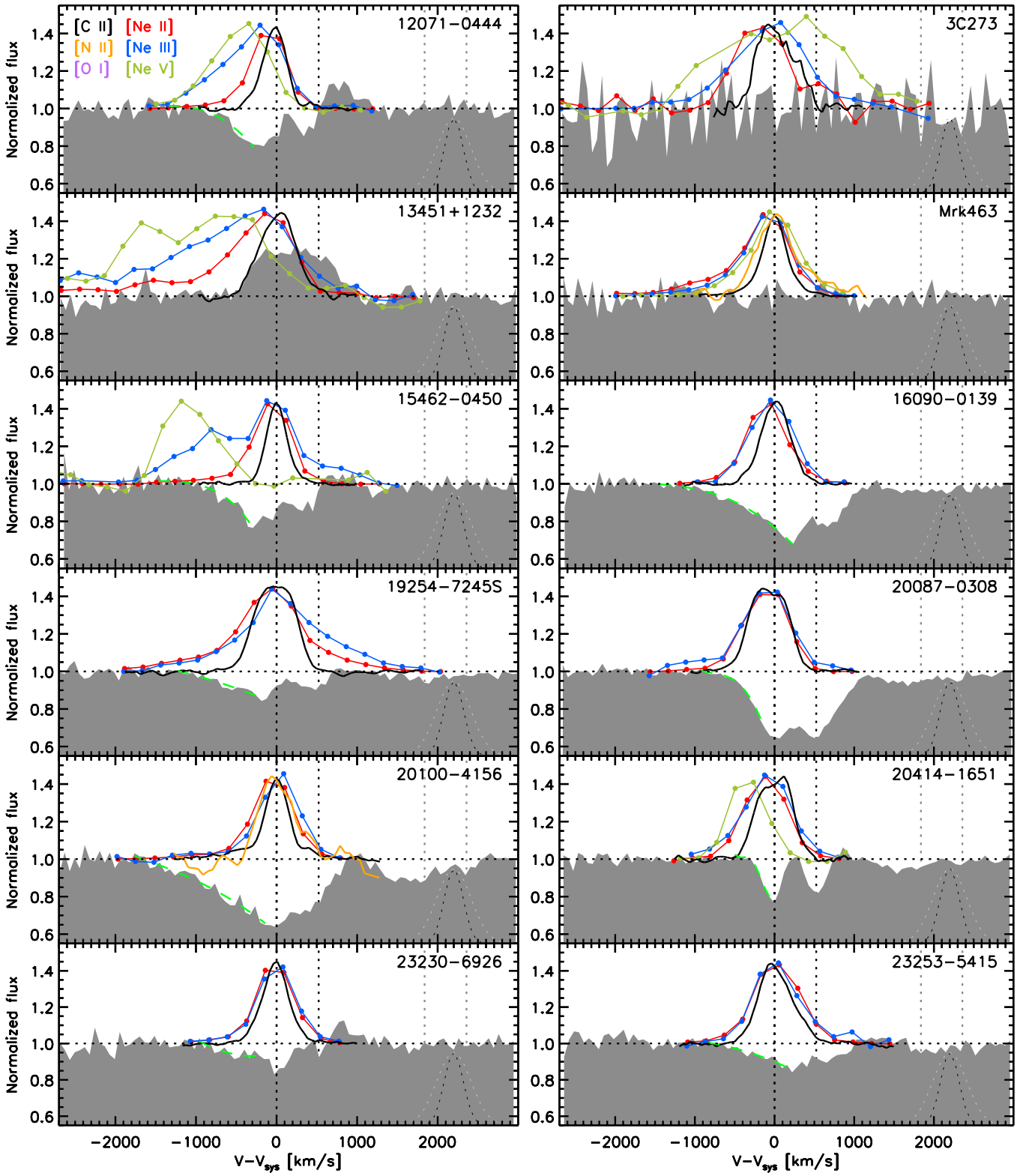

Figure 2. (Continued)

4.3. A Qualitative Analysis of the OH119 Profiles

4.3.1. An Idealized Outflow Model

P-Cygni line profiles are powerful diagnostics of outflow kinematics. Given the prevalence of P-Cygni type profiles among our sample of OH119 spectra, we explore a general explanation for our observations along the lines of a spherically symmetric, optically thin, accelerating outflow. In our model, we assume pure radiative excitation and de-excitation in a two-level system, i.e., pure scattering and no extinction. The effects of extinction will be considered later. In this idealized system (Figure 4), the absorption in the outflow arises in the "tube" (F) in front of the far-IR continuum source (the nucleus), where radially outflowing OH molecules in the ground state absorb

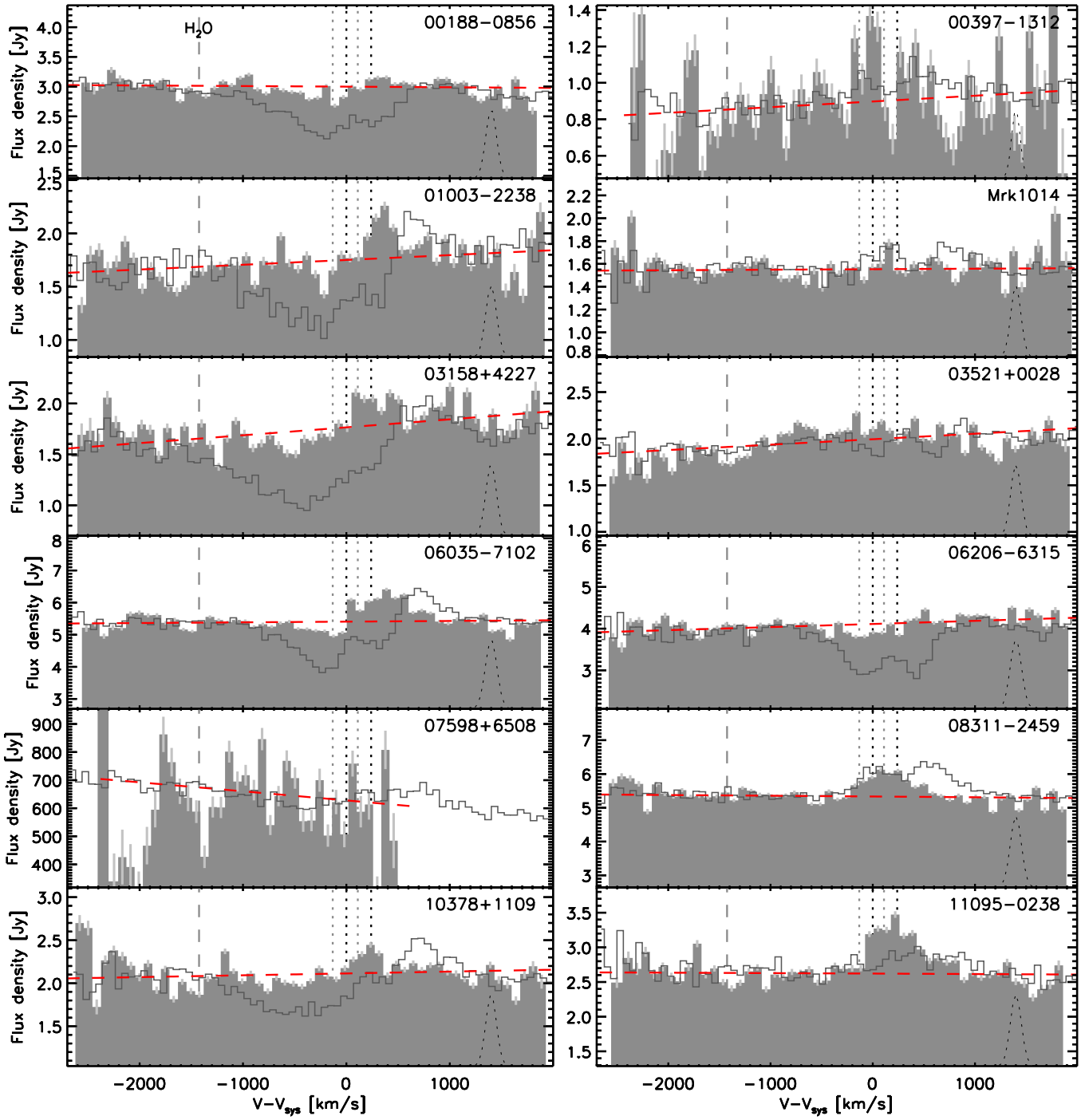

Figure 3. *Herschel*-PACS spectra (gray surfaces) of the unresolved blend of the 79 μm OH and ^{18}OH doublets for ULIRGs observed in the HERUS survey. All spectra have the same flux dynamic range. Systemic velocity is defined as the rest wavelength of the OH $\Pi_{1/2}$ – $\Pi_{3/2}$ $(1^-/2)$ – $(3^+/2)$ transition at 79.118 μm. The rest velocities of the 79 μm ^{16}OH and ^{18}OH lines (see Table 3) are indicated by black and gray dotted vertical lines, respectively. Also indicated, as a gray dashed vertical line, is the rest velocity of the H_2O 4_{23}–3_{12} transition (78.742 μm; at $v = -1425$ km s^{-1}). The adopted local continuum is shown in red. Overlaid also are the normalized OH119 profiles (dark gray histogram lines), scaled to the 79 μm wavelength range using the adopted 79 μm continuum. The spectral resolution at 79 μm is shown by a dashed black Gaussian profile in the bottom right corner of each panel.

(A color version of this figure is available in the online journal.)

radially emitted 119 μm continuum photons. Like elsewhere in the outflow (which we will refer to as the "halo" (H) from here on out), the absorption is followed by reemission[23] of the photon. The chances of a reemitted continuum photon continuing along the same radial path are small, given the isotropic nature of radiative deexcitation. The net observed result will hence be a blueshifted absorption trough with velocities ranging from zero to $-v_{\rm max}$, the highest blueshifted velocity in the outflow.

All other parts of the outflow (the "halo") contribute with emission components to the profile, resulting from the isotropic

[23] Instead of reemission of a 119 μm photon, the capture of an 84 μm photon can excite the molecule to the next higher excited level in the $\Pi_{3/2}$ branch. The chances of this process occurring increase with 84 μm photon density, and thus with proximity to the far-IR nucleus.

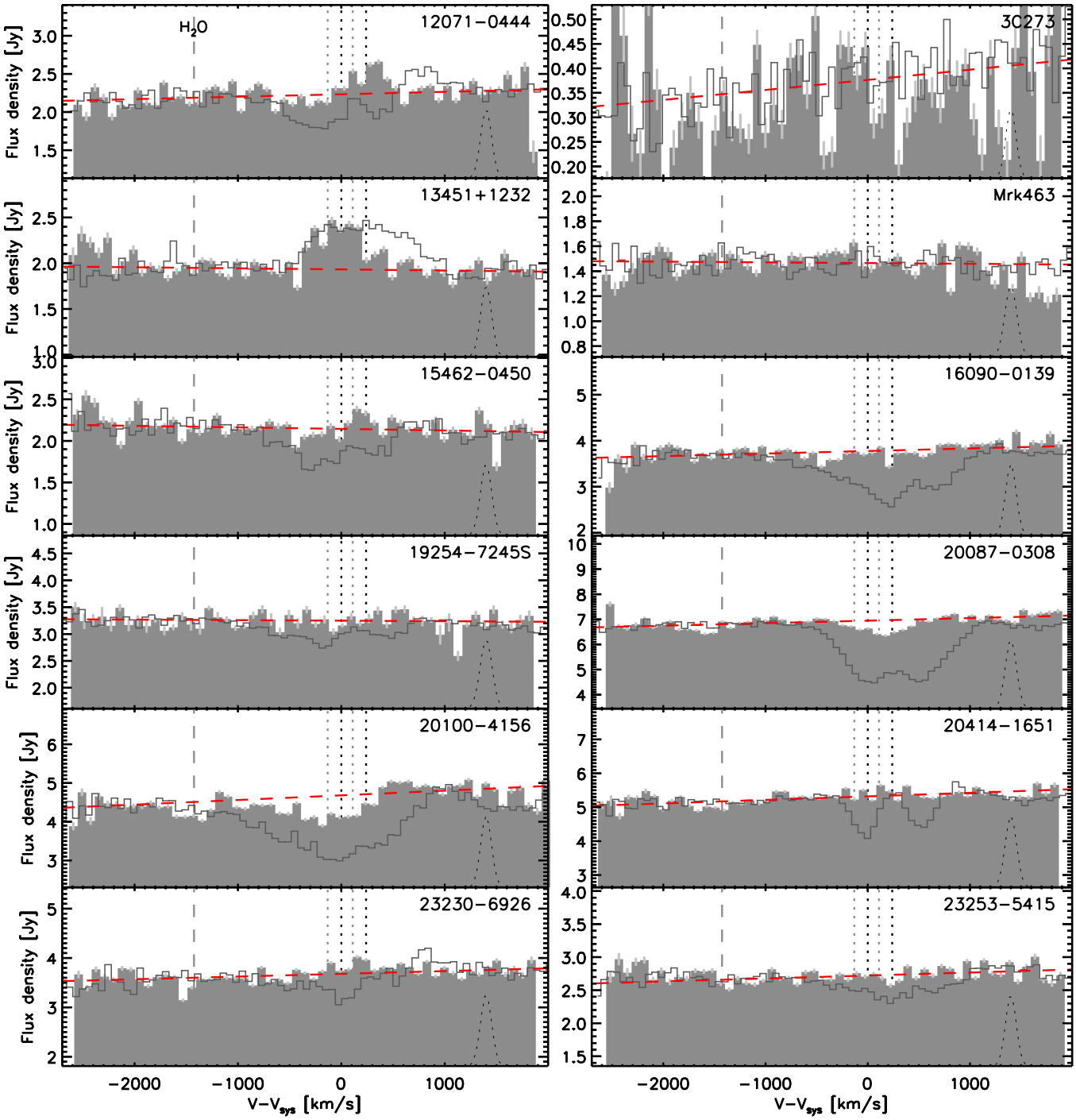

Figure 3. (Continued)

reemission of 119 μm photons that were absorbed on their radial paths by OH molecules in the outflow. The line-of-sight velocities sampled by the emission component range between $+v_{\rm max}$ and $-v_{\rm max}$, resulting in a symmetric emission profile centered on zero velocity.

In the absence of extinction and occultation, as per our assumptions, none of the continuum photons from the central source will be lost. The photons are merely scattered into or out of the line of sight to the observer. Since every observer must see the same line profile under our assumption of isotropy, this result then implies that the number of photons scattered out of the line of sight must be equal to the number of photons scattered into the line of sight, or else some observers would see more emission than absorption, or vice versa. The net observed result of the interaction of 119 μm continuum photons with outflowing OH molecules will thus only be a change in the velocity distribution of these photons between $-v_{\rm max}$ and $+v_{\rm max}$ (see also González-Alfonso et al. 1998, 2013), since the total flux is effectively conserved.

4.3.2. Problems with Idealized Outflow Model

In practice, however, none of our OH119 P-cygni profiles display an emission component that is as strong as the absorption component. In most sources, the emission component is clearly

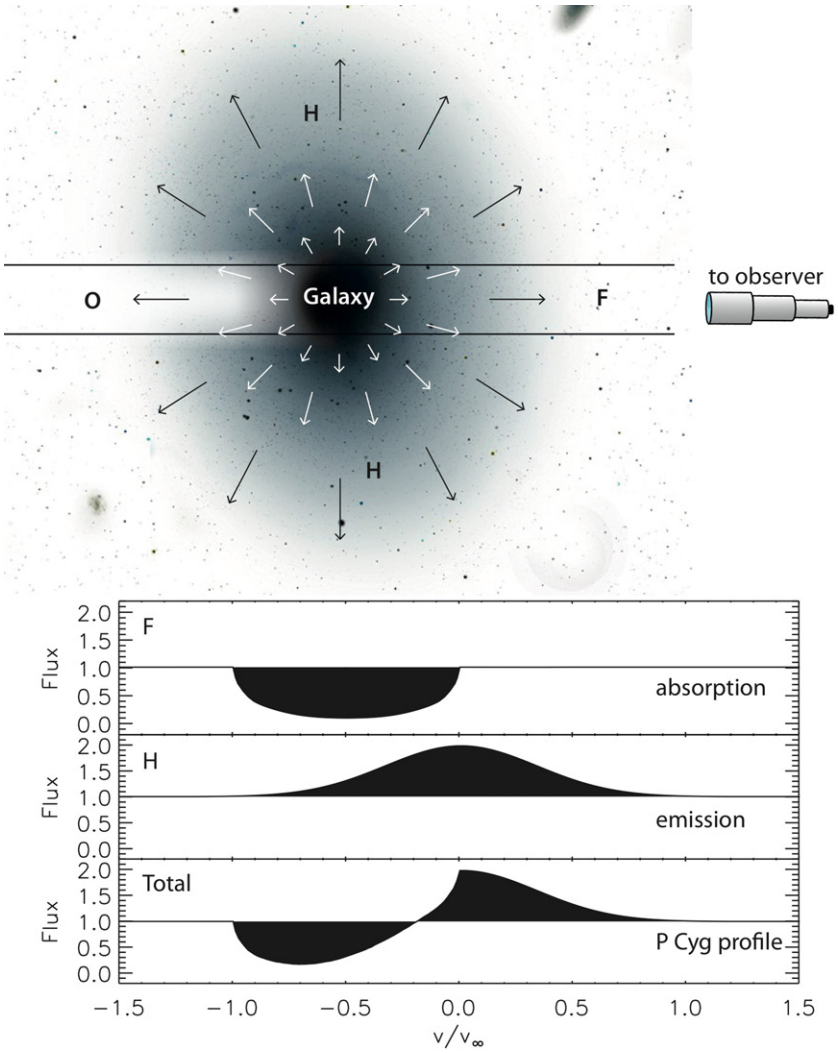

Figure 4. Top panel: the geometry of a spherically symmetric outflow with outward increasing velocity. We distinguish four different components: the galactic nucleus, the "tube" in front of the nucleus (F), the occulted/attenuated "tube" behind the galaxy's nucleus (O), and the "halo" around the nucleus (H). Bottom panel: A P-Cygni profile arises from four spectral components: gas in the front tube (F) absorbing the continuum spectrum of the galaxy's nucleus is co-added to the emission contributed by the halo (H) and any attenuated emission seeping through from the rear "tube" (O). The profile depicted is for a single line. In the case of the OH119 and OH79 doublets, two line profiles, 520 and 240 km s^{-1} apart, respectively, need to be co-added. This fact severely complicates the interpretation of the observed spectral profile. Figure adapted from Lamers & Cassinelli (1999).

(A color version of this figure is available in the online journal.)

weaker than the absorption component. In these sources extinction may suppress part of the "halo" emission from reaching the observer, especially the "halo" component originating from behind the dusty nucleus (labeled the "occultation zone" ("O") in Figure 4). This result would especially suppress the most redshifted emission (close to $+v_{\rm max}$). The latter may be seen most clearly in IRAS 01003−2238, where the blue absorption wing of the 119.233 μm OH line extends about 700 km s^{-1} beyond the red emission wing of the other (119.441 μm) doublet line. Also, absorption by CH^+ (at $v = +1543$ km s^{-1}) may contribute to the suppression (e.g., IRAS 03158+4227).

A close connection between the OH119 profile shape and obscuration is indeed implied by a comparison of the equivalent width of the OH119 profile, EQW(OH119), and the silicate strength $S_{\rm sil}$ (Spoon et al. 2007). According to our outflow model, EQW(OH119) should be zero in the absence of extinction. We show this comparison in Figure 5, where we see a clear trend of decreasing OH119 emission relative to OH119 absorption as the silicate obscuration increases ($S_{\rm sil}$ becomes more negative). This result indicates that the obscuring geometry strongly affects the emergence of the OH119 emission component and that, at the very least for the most deeply obscured ULIRGs in our sample, the OH119 emission region is located within the buried nucleus, consistent with radiative excitation being the principal source of OH excitation. This result also indicates that for the most strongly affected sources, not only the 119 μm continuum but also the 79 μm continuum will be optically thick.

Two sources in our sample are clear outliers in Figure 5: IRAS 00397−1312 and 11095−0238. Both are deeply obscured and only show OH119 emission components. Their OH119 pure emission profiles, along with those of IRAS 08311−2459, IRAS 13451+1232, and Mrk 1014, cannot be explained by our model. In principle, in these sources the upper level of OH119 can be collisionally rather than radiatively excited to produce the double emission profile. The emitting gas would hence have to reside in warm, dense molecular clouds (Spinoglio et al. 2005).

There are many factors which likely condemn our outflow model to be an oversimplification of the true OH kinematics. For instance, the OH119 lines are mostly optically thick, meaning

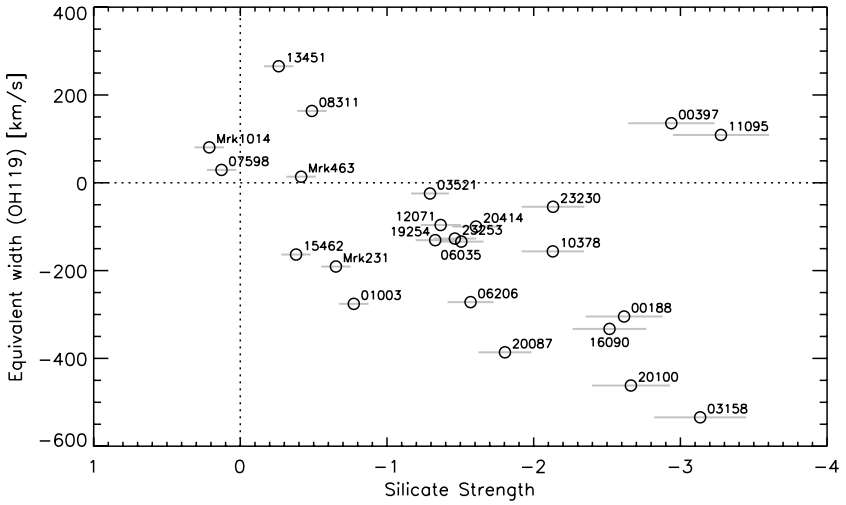

Figure 5. Equivalent width of the OH119 feature as a function of silicate optical depth (Spoon et al. 2007). A negative equivalent width implies that the OH119 absorption component is stronger than the OH119 emission component. A positive silicate strength implies that the 9.8 μm silicate feature is in emission. Our idealized model requires the equivalent width to be zero in the absence of extinction.

that they do not give an accurate account of how the OH column density is distributed over the various velocity components (^{18}OH120 is optically thin). The outflow may also deviate drastically from spherical symmetry and may be confined to outflow cones instead. This fact would introduce orientation and filling factor effects with consequences for both the observed line-of-sight velocity field and the relative strength of the emission and absorption components. For instance, an outflow with a cone axis directed toward the observer would have a dominant "tube" component with less "halo" emission than in a spherically symmetric outflow (e.g., IRAS 06206−6315). In addition, we would expect to see the full outflow velocity field. In practice, it will be hard to distinguish this scenario from the obscuration effects discussed earlier. Similarly, an outflow directed in the plane of the sky would result in "halo" emission that is strong compared to the "tube" component. The OH gas would then have to display minimal line-of-sight velocities, consistent with a mainly tangential velocity field (e.g., IRAS 13451+1232).

Even more complex scenarios may have to be invoked to explain the existence of redshifted absorption in combination with blueshifted absorption, like that seen in IRAS 16090−0139. It is possible that the line-of-sight absorption traces a slow inflow in combination with a fast outflow in this source.

A question that remains is why only 5/24 sources in our sample show pure OH119 emission profiles, two of which are sources with strong silicate obscuration (IRAS 00397−1312 and IRAS 11095−0238).

4.4. Maximum OH119 Outflow Velocity ($v_{\rm max}$) and Balnicity

Theoretical studies of the ram pressure exerted by supernova-heated winds and radiation pressure exerted on dust grains by clusters of OB stars and AGN accretion disks predict that the power of these wind acceleration mechanisms crudely correlates with the maximum velocity of the outflowing gas. The determination of the maximum gas velocity in an outflow is hence of great diagnostic value.

Both the doublet nature of the OH119 line and the proximity of the ^{18}OH120 doublet complicate a straightforward determination of the maximum outflow velocity ($v_{\rm max}$) of the OH gas. The only OH119 doublet line from which we can measure $v_{\rm max}$ without having to take into account contamination by another doublet line is the 119.233 μm line, and even for this line it is only the bluest 500 km s^{-1} that is free of contamination by the other (119.441 μm) doublet line.

Here, we define the maximum outflow velocity $v_{\rm max}$ as the velocity at which a B-spline fit to the blue absorption wing of the normalized OH119 profile intercepts the continuum. This definition is different from that used by the SHINING team (Sturm et al. 2011), who obtained their value of $v_{\rm max}$ as part of their model fit to several transitions between multiple levels of the OH molecule. Similar observations of transitions between excited OH levels do not exist for the HERUS sources. For Mrk 231, the results of the two methods agree within their uncertainties: $v_{\rm max} = 1400 \pm 150$ km s^{-1} using the SHINING method (Fischer et al. 2010) and $v_{\rm max} = 1573 \pm 200$ km s^{-1} using ours. The B-spline fits for our sample are shown in Figure 2 as green dashed curves. The resulting maximum outflow velocities are tabulated in Table 4. We estimate the uncertainty in our measured maximum outflow velocity to be $\pm$200 km s^{-1}, reflecting the uncertainty in continuum placement, the S/N of the spectrum, and the adopted value for the turbulent velocity (100 km s^{-1}). Three ULIRGs in our sample have maximum outflow velocities comparable to or exceeding that of Mrk 231. The OH119 profiles of these three sources, IRAS 00188−0856, 03158+4227, and 20100−4156, are compared to the OH119 profile of Mrk 231 in Figure 6.

Following Weymann et al. (1991) in concept, we further determine the "balnicity" for those sources in our sample with pronounced OH119 absorption troughs. Here, we define the balnicity as the integrated normalized flux $F(v)$ below the 98% flux level at velocities more blueshifted than −200 km s^{-1}:

$$B(\mathrm{km\ s^{-1}}) = \int_{-v_{\rm max}}^{-200} \left[1 - \frac{F(v)}{0.98}\right] C\, dv. \quad (1)$$

The constant C is zero except for the velocity range in which the normalized flux $F(v)$ is lower than 0.98, where C is unity. The balnicity is hence very similar to the equivalent width between two indicated velocities. The rationale that contributions to the balnicity should only be counted for velocities more blueshifted than −200 km s^{-1} is that this method excludes OH gas at rest. Also, our choice of 98%

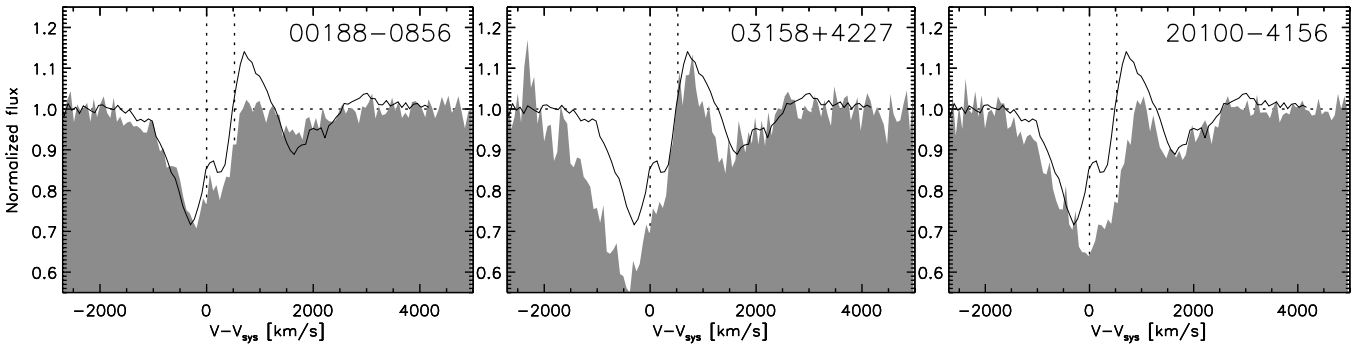

Figure 6. Comparison of the normalized OH119 profiles of IRAS 00188−0856, 03158+4227, and 20100−4156 (gray surfaces) with the OH119 profile of Mrk 231 (black line; Fischer et al. 2010).

Table 4
Quantities Measured from the OH119 Absorption Component

Galaxy	v_{max}^{obs} [a] (km s^{-1})	v_{max} [b] (km s^{-1})	Balnicity (km s^{-1})
00188−0856	−1805	−1781	118
00397−1312			
01003−2238	−1272	−1238	194
Mrk 1014			
03158+4227	−2065	−2044	350
03521+0028	−232	>−100	<1
06035−7102	−1155	−1117	81
06206−6315	−805	−750	31
07598+6508	−1225	−1190	15
08311−2459			
10378+1109	−1332	−1300	149
11095−0238			
12071−0444	−967	−922	53
3C273			
13451+1232			
Mrk 463			
15462−0450	−972	−927	61
16090−0139	−1451	−1422	53
19254−7245	−1163	−1126	39
20087−0308	−864	−812	24
20100−4156	−1635	−1609	177
20414−1651	−249	>−100	2
23230−6926	−894	−845	20
23253−5415	−712	−650	8
Mrk 231[c]	−1594	−1573	120

Notes. The estimated uncertainty for all v_{max} velocities is ±200 km s^{-1} the estimated uncertainty for the balnicity is 15%.
[a] Terminal velocity as observed.
[b] Terminal velocity corrected for turbulence (100 km s^{-1}) and spectral resolution in quadrature.
[c] SHINING source (Fischer et al. 2010) processed using our methods.

of the normalized continuum as the cut-off for integrating the absorption profile is rooted in the uncertainty in our choice of the continuum level. Excluding the first 2% of the absorption feature therefore ensures that we are never integrating a "false" absorption. The resulting balnicities have an estimated uncertainty of 15% and are tabulated in Table 4. Five ULIRGs have balnicities comparable to or exceeding that of Mrk 231.

4.5. Correlations of v_{max} and Balnicity with Other Observables

Here, we follow the SHINING team (Sturm et al. 2011) and look for a correlation between the maximum OH119 outflow velocity and measures of the power of the AGN and the starburst. To infer the power of the AGN in a ULIRG, we measure the slope of the mid-IR continuum between 15 and 30 μm and use the zero-point calibration from Veilleux et al. (2009) to convert the relative AGN contribution to L_{bol}, α, to the bolometric AGN luminosity $L_{AGN,bol}$. We estimate the uncertainty in α to be ±0.15.

L_{bol} itself is assumed to be $1.15 \times L_{IR}$, which Veilleux et al. (2009) deem appropriate for ULIRGs. The star formation rate (SFR) is inferred from the fraction of L_{IR} that is not powered by the AGN, $1-\alpha$, and is defined as SFR $= (1-\alpha) \times 10^{-10}\ L_{IR}$ (Sturm et al. 2011).

In Figure 7, we plot the maximum outflow velocity for 17 out of 24 of our sources as a function of AGN luminosity and SFR. Also shown is Mrk 231, the SHINING source (Fischer et al. 2010) that we analyzed in the same way as the HERUS sample. The upper panel of Figure 7 suggests a trend of increasing maximum OH outflow velocity with increasing AGN power. The trend appears steeper for sources with a high silicate optical depth than for sources with a lower silicate optical depth. All four starburst-dominated sources (color coded blue) furthermore show maximum outflow velocities below ∼800 km s^{-1}, while all four AGN-dominated sources (color coded green) display maximum outflow velocities in excess of 900 km s^{-1}. The lower panel of Figure 7 is a scatter plot, suggesting no correlation between $f(30\,\mu m)/f(15\,\mu m)$ based SFR and the maximum OH outflow velocity in our sample. A similar lack of correlation is obtained using a polycyclic aromatic hydrocarbon (PAH) flux based SFR (Farrah et al. 2007, their Equation (5)). The above findings are consistent with the results presented by Sturm et al. (2011) for a sample of six ULIRGs and one starburst galaxy observed in the OH119, OH79, and OH65[24] doublets.

As shown in Figure 8, a correlation also appears to exist between the AGN luminosity and the balnicity of the OH119 doublet. Apart from a few notable outliers, the power law correlation holds over a factor of four in AGN luminosity. This result may be surprising since the OH119 doublet is generally optically thick and thus the depth of the feature is not necessarily a true measure of the OH column probed. Outliers in this plot, IRAS 10378+1109, 12071−0444, 16090−0139, Mrk 231, and especially IRAS 07598+6508, happen to also be outliers in the top panel of Figure 7. The trends in both plots would improve if the AGN fraction α was underestimated beyond our adopted uncertainty of 15% for IRAS 10378+1109 ($\alpha = 0.30$) and overestimated for IRAS 12071−0444 ($\alpha = 0.75$), 16090−0139 ($\alpha = 0.43$), and Mrk 231 ($\alpha = 0.81$). For

[24] Transition between the second and third excited states on the $\Pi_{3/2}$ ladder of OH. The doublet lines are centered at 65.132 and 65.279 μm, respectively.

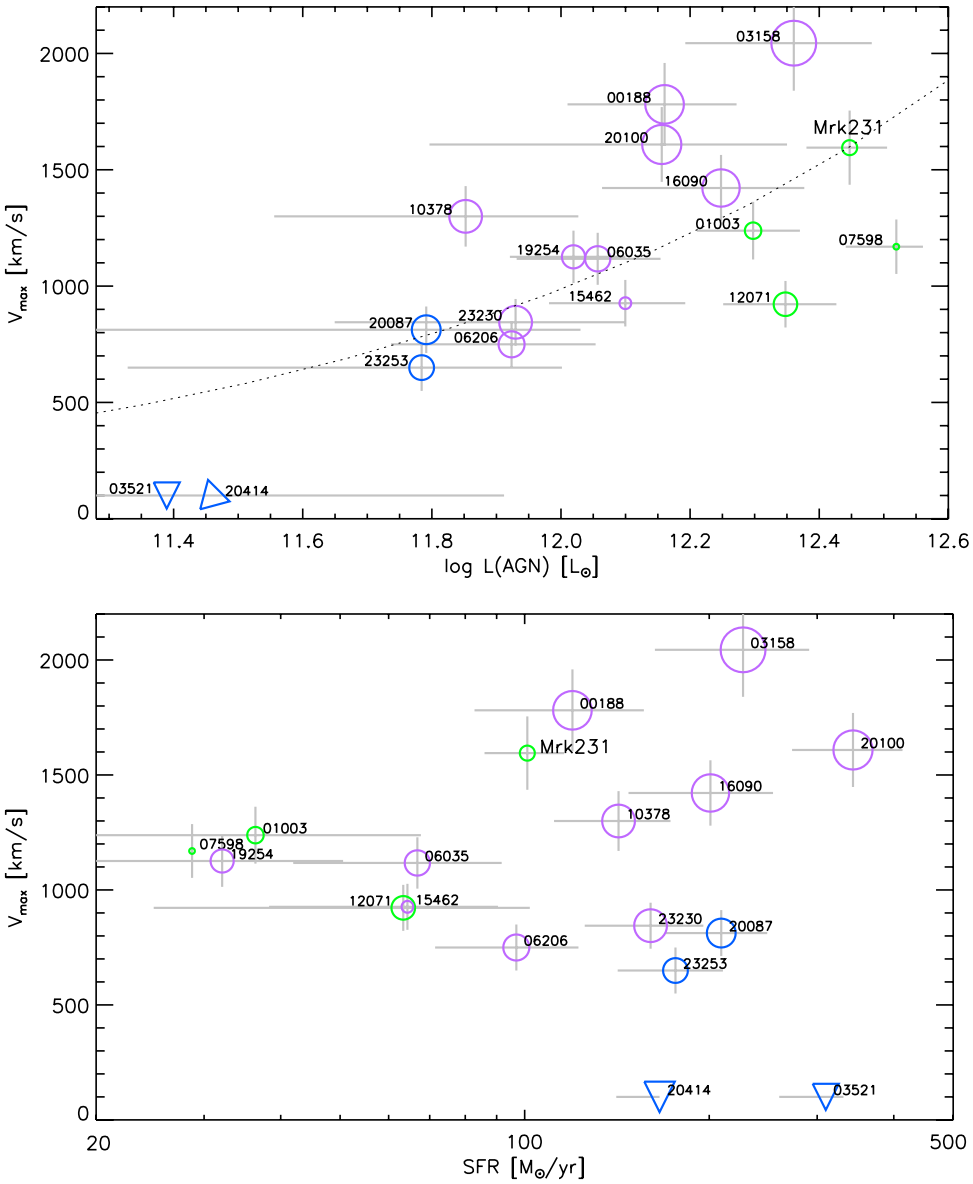

Figure 7. Upper panel: maximum OH119 outflow velocity as a function of AGN luminosity. The circle size is proportional to the silicate optical depth of the target. Triangles indicate upper limits. The dotted line is a power-law fit to all but two sources: IRAS 03521 and 20414. The power law has the form $\log(v_{\rm max}/{\rm km\ s^{-1}}) = -2.64(\pm1.80) + 0.47(\pm0.15) \times \log(L_{\rm AGN}, {\rm bol}/L_{\odot})$. Lower panel: maximum OH119 outflow velocity as a function of SFR. In both panels, starburst-dominated sources ($\alpha < 0.25$) are shown in blue, AGN-dominated sources ($\alpha > 0.75$) are shown in green, and intermediate sources are shown in purple.

(A color version of this figure is available in the online journal.)

IRAS 07598+6508, no plausible change in the AGN fraction can bring this source in agreement with the general trend. Also, an unfortunate choice of the local continuum offers no explanation for this source's shallow OH119 absorption component. Perhaps IRAS 07598+6508 has more in common with the three high-luminosity ULIRGs lacking OH119 absorption components, and which therefore are missing from the above analyses: IRAS 00397−1312, 08311−2459, and Mrk 1014. Like IRAS 07598+6508, all three ULIRGs are clearly AGN-dominated based on their estimated AGN fractions (Table 2).

Note that based on balnicity, IRAS 01003−2238, and not IRAS 00188−0856, would be the second most extreme OH119 outflow source behind IRAS 03158+4227.

In Figure 9, we show the distribution of HERUS sources in the mid-IR diagnostic diagram of 6.2 μm PAH equivalent width (EQW62) versus silicate strength ($S_{\rm sil}$), the so-called fork diagram (Spoon et al. 2007). This diagram separates sources dominated by AGN clumpy hot dust emission (class 1A) from sources dominated by star formation (class 1C) and sources dominated by a deeply buried nucleus (class 3A). Most sources are found along two branches connecting these three extremes. The 24 sources of the HERUS sample are distributed quite evenly along these branches and are shown as red circles and squares. In the upper panel, the circle size is proportional to the measured maximum OH119 outflow velocity ($v_{\rm max}$), while the red squares denote HERUS sources lacking an OH119 absorption component. As can be seen in the upper panel, in our sample $v_{\rm max}$ is highest among ULIRGs harboring a deeply buried nucleus and lowest among ULIRGs with a starburst-like mid-IR spectral appearance. HERUS ULIRGs in quadrant 1A of the diagram (i.e., AGN-dominated sources) show moderately high OH outflow velocities. Here and in quadrant 1B, which together constitute the AGN-dominated branch, we find a higher fraction of sources lacking an absorption component in their OH119

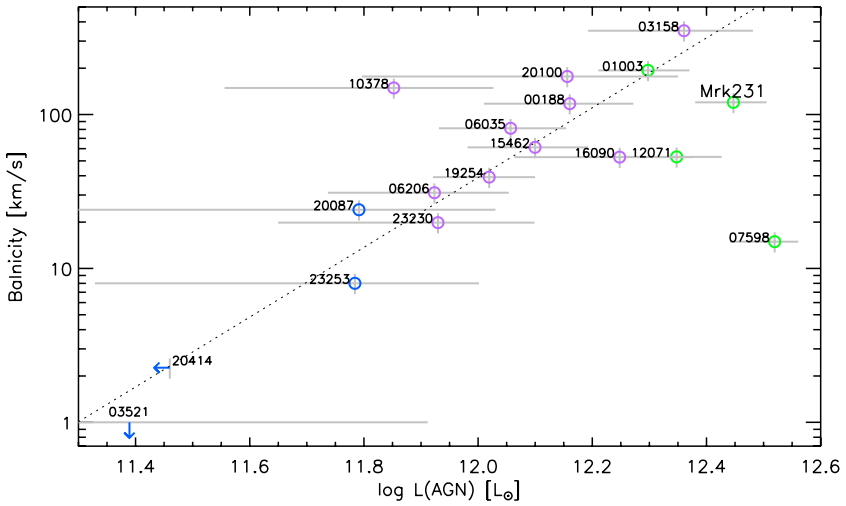

Figure 8. Balnicity of the OH119 absorption profiles as a function of AGN luminosity for our sources. Not shown are sources with pure emission features. The dotted line is a power-law fit to all but three sources: IRAS 03521, 07598, and 20414. The power law has the form $\log(B/\mathrm{km\ s^{-1}}) = -25.6(\pm9.6) + 2.27(\pm0.79) \times \log(L_{\mathrm{AGN}}, \mathrm{bol}/L_{\odot})$. Starburst-dominated sources ($\alpha < 0.25$) are shown in blue, AGN-dominated sources ($\alpha > 0.75$) are shown in green, and intermediate sources are shown in purple.

(A color version of this figure is available in the online journal.)

feature than on the obscuration-dominated branch (quadrants 2B+2C and 3A+B). In the bottom panel of Figure 9, circle sizes are a measure of the highest blueshifted velocities of ionized gas seen in the emission lines of 15.56 μm [Ne III] and 14.32 μm [Ne V] (Spoon & Holt 2009). The velocities are computed as the line center velocity shift at 10% of the peak flux (VC10) minus half of the full width at 10% of the peak flux. The results are shown only for those sources in our sample that display a genuine outflow wing. The criterion for the latter is a VC10 line center blueshift of at least 150 km s^{-1} (see also Section 4.6). As can be seen in this panel, the highest outflow velocities are found among the HERUS sources in quadrant 1A.

Spoon et al. (2007) proposed that the strong silicate obscuration of ULIRGs on the upper branch of the fork diagram implies that these sources have not yet shed their obscuring molecular cocoon that was created during the earlier stages of the galaxy interaction. In the fork diagram, the evolutionary path that an energetically dominant buried AGN would take to evolve from the upper branch (quadrant 3A or 3B) to the locus of unobscured AGNs (quadrant 1A) would be almost vertical if the disruption/dispersion of the molecular cocoon by an AGN-driven wind would expose the hot dust of the decloaking AGN. The additional strong mid-IR continuum emission would dilute the remaining starburst signatures and lower both the apparent silicate optical depth (i.e., increase S_{sil}) and the 6.2 μm PAH equivalent width. The predominance of high *molecular* gas outflow velocities on the upper branch and the predominance of high *ionized* gas outflow velocities on the lower branch would be consistent with this evolutionary scenario: the molecular cocoon needs to be sufficiently dispersed for the ionized gas outflow interior to it to become visible to us.

4.6. Comparison to MIR–FIR Fine-structure Line Profiles

4.6.1. Mid-IR Neon Line Profiles

A survey of 82 galaxy-integrated *Spitzer*-IRS spectra of ULIRGs has revealed that the emission line profiles of ionized neon gas show clear departures from virial gas motion in a sizeable fraction (28/82) of ULIRGs (Spoon et al. 2009; Spoon & Holt 2009). The departures are both in the form of blue wings and blueshifts of the three strongest mid-IR neon lines, 12.81 μm [Ne II], 15.56 μm [Ne III], and 14.32 μm [Ne V]. This result suggests decelerating ionized gas outflows in a stratified medium photoionized by the central source as the most likely explanation (Spoon & Holt 2009). In Figure 2, we overlay the normalized neon line profiles onto the normalized OH119 profiles (in so far as these lines are detected and have reasonable S/N) to facilitate comparison of the kinematics of the molecular gas to those of the ionized gas.[25] Note that the spectral resolution of the *Spitzer*-IRS observations is about half of that of the OH119 observations ($\Delta v \sim 500$ and 250–300 km s^{-1}, respectively).

4.6.2. [C II] Line Profiles

Also overlaid in Figure 2 are the line profiles of the 158 μm [C II] fine-structure line, which are detected in all sources in our sample. Other FIR fine-structure lines in our program are less frequently and less well detected. The brightest of these other lines, 63 μm and 145 μm [O I] and 122 μm [N II], do not show line shifts, broad line wings, or line asymmetries as far as we are able to assess given the limited S/N of these spectra. [C II], in contrast, does show departures from pure Gaussian profile shapes. Some of these profiles take the form of small line center shifts of less than 100 km s^{-1} (IRAS 00188−0856 and 01003−2238), while others take the form of subtle blue or red wing asymmetries (IRAS 12071−0444 and 23253−5415, respectively). Broad [C II] emission components are seen in several sources. In Mrk 463, about half the flux is associated with a Gaussian component with FWHM$_B \sim 600$ km s^{-1}. In four other sources, the broad component (B) is harder to discern, and has less flux associated with it (Figure 10). These sources are IRAS 01003−2238 (FWHM$_B = 1150$ km s^{-1}), IRAS 06035−7102 (FWHM$_B = 800$ km s^{-1}), IRAS 11095−0238 (FWHM$_B = 900$ km s^{-1}), and IRAS 20100−4156 (FWHM$_B = 1000$ km s^{-1}). See also Section 4.7. The broadest [C II] lines in our sample overall are seen in IRAS 19254−7245 and IRAS 20087−0308. Both lines are flat-topped, have FWHMs of approximately 600 km s^{-1}, and require two Gaussian components for a good line profile fit.

[25] The three neon lines together span a range of 21–97 eV in ionization potential.

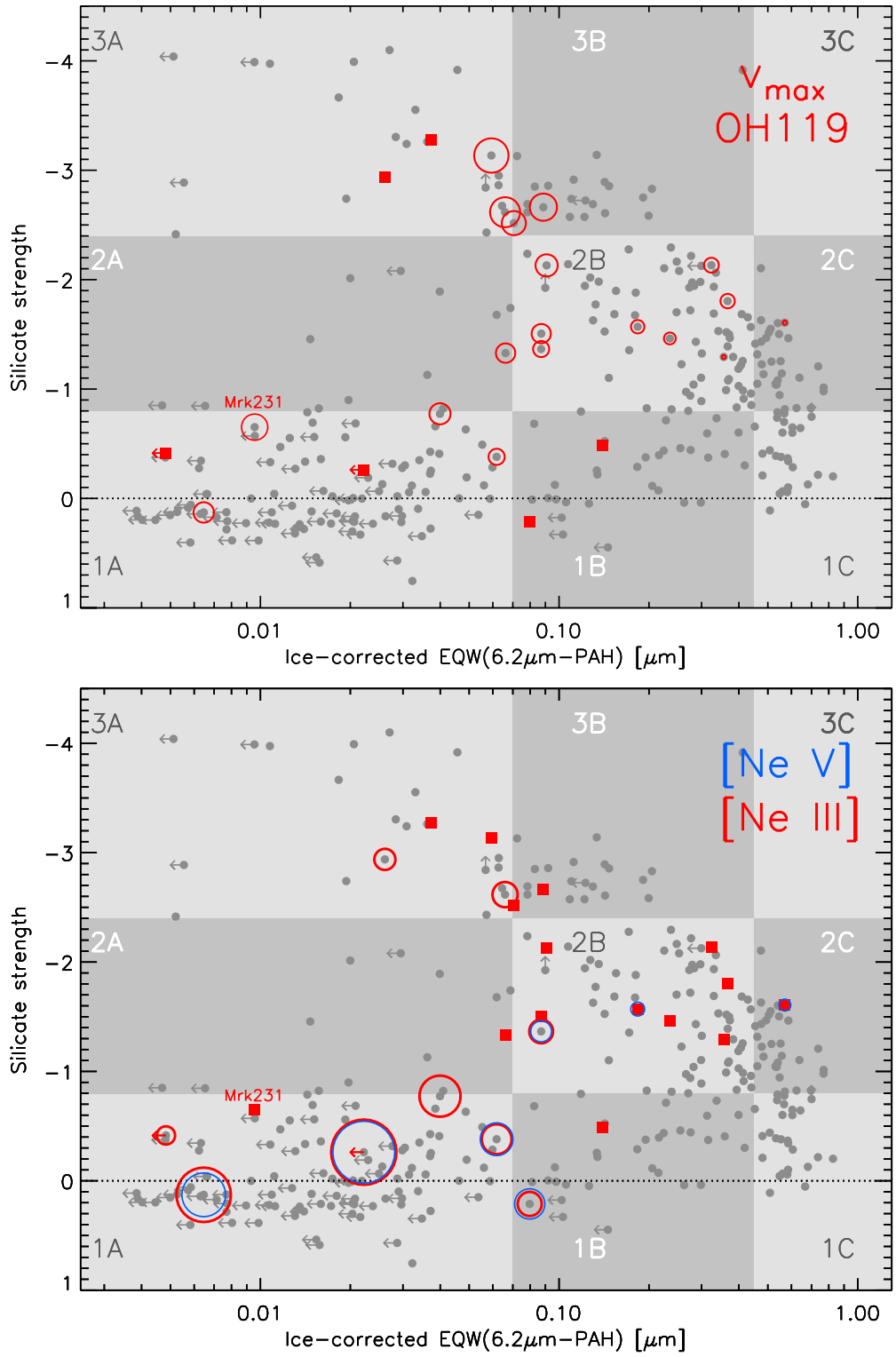

Figure 9. Diagnostic plot of the 9.7 μm silicate strength vs. the equivalent width of the 6.2 μm PAH emission feature (Spoon et al. 2007). Upper and lower limits are denoted by arrows. The galaxy spectra are classified into nine classes (identified by nine shaded rectangles) based on their position in this plot. From class 1→2→3, the silicate absorption feature increases in strength, while from class A→B→C the equivalent width of the 6.2 μm PAH emission feature increases. Top panel: circle sizes (red) are proportional to the maximum OH119 outflow velocity (v_{max}) inferred from the blueshifted absorption wing. Sources shown as red squares lack an OH119 absorption component from which to infer v_{max}. Bottom panel: circle sizes are proportional to the blue wing velocity at which the neon line profile (15.56 μm [Ne III] = red; 14.32 μm [Ne V] = blue) reaches 10% of the peak flux. Circles are plotted only for those sources for which the line center shift at 10% of the peak flux (VC10) is more negative than −150 km s^{-1}. Note that the [Ne V] lines are generally not detected below silicate strengths of −2.

(A color version of this figure is available in the online journal.)

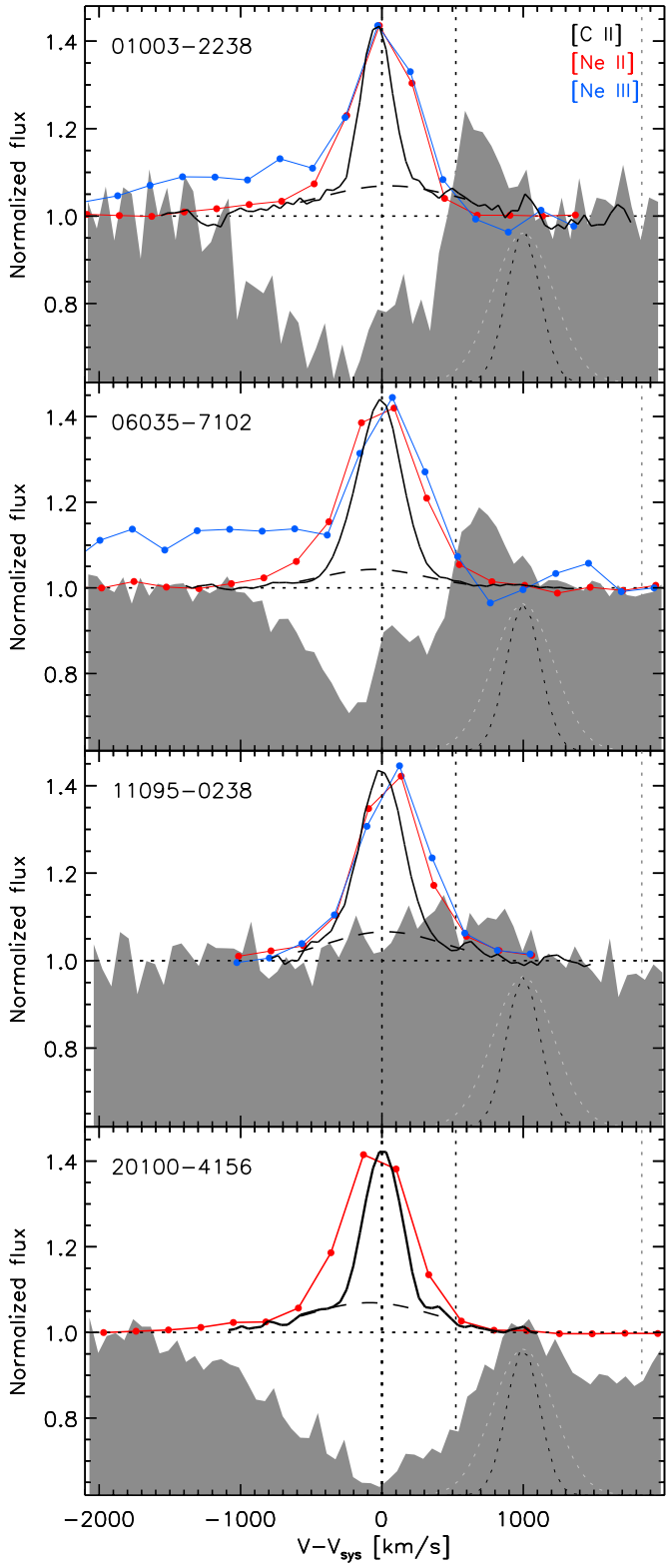

Figure 10. Comparison of the normalized 119 μm OH doublet profile to the scaled emission line profiles at 12.81 μm [Ne II] (red), 15.56 μm [Ne III] (blue), and 158 μm [C II] (black). All four sources show broad [C II] pedestal emission, consistent with a Gaussian profile of FWHM of 800–1150 km s^{-1} (black dashed lines). The spectral resolution of the OH119 line is shown by a dashed black Gaussian profile in the bottom right corner of each panel. The *Spitzer*-IRS-SH spectral resolution is shown as a light gray profile.

(A color version of this figure is available in the online journal.)

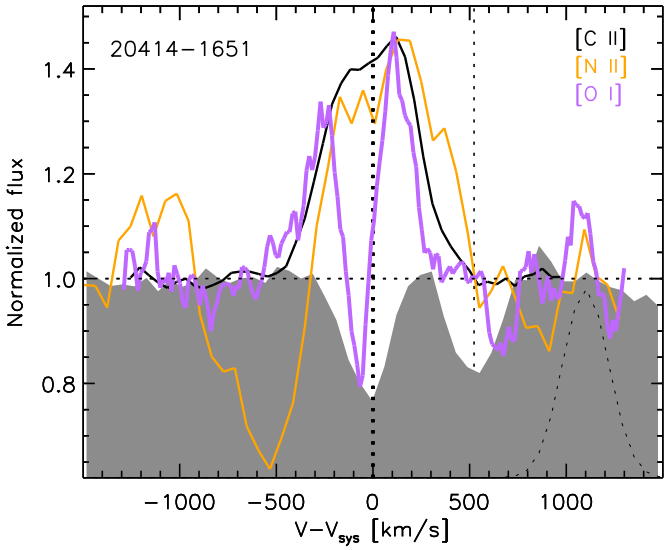

Figure 11. Comparison of the normalized 119 μm OH doublet profile to the scaled and smoothed emission line profiles of 63 μm [O I] (purple), 122 μm [N II] (orange), and 158 μm [C II] (black) lines. The strong absorption in the blue wing of the 122 μm [N II] line is likely due to outflowing o-H_2O 4_{32}–4_{23} (121.7191 μm; $v = -440$ km s^{-1}; Fischer et al. 2010). The [O I] line appears to be self-absorbed at velocities around −100 km s^{-1}. Departures from pure Gaussian behavior can also be seen in [C II] and [N II] at those velocities. The spectral resolution of the OH119 line is shown by a dashed black Gaussian profile in the bottom right corner.

(A color version of this figure is available in the online journal.)

4.6.3. [N II] Line Profiles

For some sources in our sample, the 122 μm [N II] line is broader than the [C II] line—more than would be expected based on the difference in spectral resolving power between their observed wavelengths. An extreme case may be Mrk 1014, for which the intrinsic FWHMs differ by a factor of two (Figure 2). We speculate that these differences may be due to differences in critical density between the 122 μm [N II] and the [C II] lines in ionized gas, in the sense that the [N II] line may be tracing denser gas deeper in the galaxy potential well than the [C II] line does. Note that some of our 122 μm [N II] profiles are affected by absorption/emission due to the high-lying 4_{32}–4_{23} transition of o-H_2O at 121.7191 μm, 430 km s^{-1} in the blue wing of the [N II] line (Fischer et al. 2010; González-Alfonso et al. 2010), although absorption by HF at the same wavelength cannot be ruled out (Fischer et al. 2010).

The clearest and most extreme example in our sample is IRAS 20414−1651, whose [N II] line profile is shown in Figure 11 along with the line profiles of [C II], 63 μm [O I], and OH119. The same source also shows the only clear case of self-absorption of 63 μm [O I] emission in our sample, indicating that there is cold neutral oxygen gas (photodissociation regions) in the line of sight to the central region (Poglitsch et al. 1996). Another clear example of 121.7191 μm H_2O absorption is IRAS 20087−0308. H_2O *emission* is tentatively detected in IRAS 00397−1312 at almost the same strength as the [N II] line there.

4.6.4. Comparison of Fine-structure Line Profiles to OH119 Profiles

A source-by-source comparison of the galaxy-integrated fine-structure and OH119 line profiles, as visualized in Figures 2, 10, and 11, allows us to make several observations about the gas kinematics of the ionized, neutral, and molecular gas in our

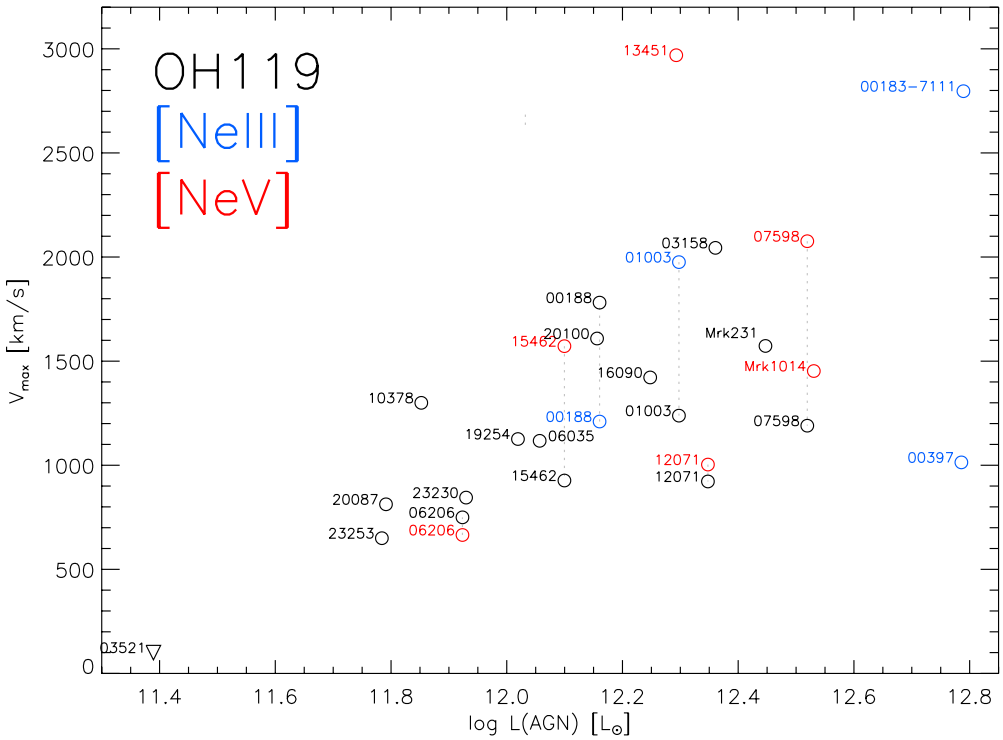

Figure 12. Maximum outflow velocity as measured for OH119 absorption profiles (black) 15.56 μm [Ne III] (blue), and 14.32 μm [Ne V] (red) emission line profiles. The OH119 data are the same as in Figure 7. Besides the HERUS sample, the plot contains the neon line measurement for IRAS F00183−7111 (Spoon et al. 2009). The triangle used for IRAS 03521+0028 indicates an upper limit on v_{max}(OH119). We estimate the uncertainty in v_{max}([Ne III]) and v_{max}([Ne V]) to be ∼15%.
(A color version of this figure is available in the online journal.)

sample of ULIRGs as seen in the far-IR. First, the far-IR fine-structure lines do not show the pronounced line asymmetries that the three mid-IR neon lines and the OH119 doublet show. Unlike the latter lines, the far-IR fine-structure line emission is likely dominated by low-velocity components that are closely tied to gas in virial motion in the galactic nuclei. Second, in 4/24 sources, the far-IR fine-structure line with the highest S/N in our sample, [C II], shows a faint symmetric pedestal that can be fit with a Gaussian profile with FWHM$_B$ = 800–1150 km s^{-1}. In three of these sources, the velocity field covered by the blue wing of the OH119 absorption is in good agreement with the extent of the [C II] pedestal and the 12.81 μm [Ne II] emission line (Figure 10). Only in IRAS 20100−4156 does the [C II] emission not extend to as large a blueshift as the OH119 absorption and the [Ne II] emission. Red wing [C II] emission appears to extend beyond the red wing of [Ne II] and the red wing of the red (119.441 μm) doublet line of OH119 in IRAS 01003−2238. This extension could point toward significant attenuation at wavelengths shorter than 158 μm on the emission originating at the far side of an outflow. Third, the highest detected blueshifted velocities probed by the [C II] line are generally far smaller than those probed by OH119. There are, however, a few cases where the (modest) maximum blueshifted velocities match: IRAS 13451+1232, 20087−0308, and 23253−5415. Fourth, equally poor correspondence is found between the blueshifted velocities probed by the three neon lines and OH119. In two-thirds of our sample, the neon lines probe higher blueshifted velocities than OH119. Only in two sources is it the other way around: IRAS 03158+4227 and 20100−4156. Note, however, the faint blue wing of [Ne II] emission in the latter source extends to almost the same maximum blueshift as OH119 (Figure 10). Wings like these easily remain hidden in lower S/N Spitzer-IRS spectra.

The comparison of the velocity profiles of OH119 to the mid-IR and far-IR fine-structure lines hence illustrates the importance of OH119 and the mid-IR neon lines as tracers of molecular and ionized gas outflows in ULIRGs. Far-IR fine-structure lines, on the other hand, appear less suitable as outflow tracers, as they are much more strongly dominated by gas in virial motion than the neon lines and the OH119 absorption profiles. Excellent S/N is hence required to be able to reveal high-velocity wings in far-IR fine-structure lines. In our sample, only 4/24 sources met this criterion.

Interestingly, the velocity field covered by the blue wing of the OH119 absorption is in good agreement with the extent of the blue wing of the [C II] and 12.81 μm [Ne II] emission lines in three out of four sources (Figure 10). Only in IRAS 20100−4156 does the [C II] emission not extend to as high a blueshift as the OH119 absorption and the [Ne II] emission.

A different picture emerges if we define a maximum outflow velocity for the 15.56 μm [Ne III] (blue) and 14.32 μm [Ne V] lines and compare their maximum outflow velocities to those of the OH119 data. We define the maximum neon line outflow velocity (v_{max}(Ne)) as the velocity at which the blue wing of the emission line profile reaches 10% of the peak of the line profile. This quantity is defined only for those line profiles that exhibit a clear blue wing or line profile shift at 10% of the peak of the profile (VC10). A comparison between the maximum outflow velocities for the molecular and ionized gas outflows is shown in Figure 12.

While neither the [Ne III] nor the [Ne V] results show a correlation with AGN luminosity that is tighter than the correlation found for OH119 (Figure 7), the three tracers combined do seem to map out a "zone of avoidance" in Figure 12 in which only one of our sources is found: IRAS 13451+1232. Ignoring this source for the moment, the results suggest the existence of a maximum

attainable outflow velocity at a given AGN luminosity, and this maximum value increases with increasing AGN luminosity. At AGN luminosities below $10^{12.35}$ $L_{\odot}$, the upper envelope is sampled predominantly by the molecular outflow velocities, while above $10^{12.35}$ $L_{\odot}$ it is sampled mostly by the ionized gas (i.e., the [Ne III] lines of IRAS F00183−7111 (Spoon et al. 2009) and IRAS 07598+6508). The existence of a maximum attainable outflow speed rather than a noisy correlation of $v_{\rm max}$ and $L_{\rm AGN}$ may be a natural result of projection effects of the outflows due to the random orientation of the molecular and ionized gas outflows within our sample.

The source "violating" the zone of avoidance in Figure 12, IRAS 13451+1232, cannot be reconciled with the trend by increasing the fraction of its L(IR) powered by the AGN, as this fraction is already very high ($\alpha = 0.82$). While this fact may completely disprove the concept of a maximum attainable outflow speed at a given AGN luminosity, IRAS 13451+1232, a gigahertz peaked spectrum radio source, is known to have sub-kpc size radio jets (Holt et al. 2003), which may contribute to driving the ionized gas outflow.

4.7. Atomic Mass in the Outflow from [C II] Pedestals

Four sources in our sample show high-velocity components in their [C II] lines (Figure 10), which can be fit with Gaussian profiles of FWHM$_B$ = 800–1150 km s^{-1}. These values are at the high end of the gas velocities found for the mid-IR AGN narrow line region (NLR) tracers 14.32 μm [Ne V] and 25.89 μm [O IV] in ULIRGs (e.g., IRAS 05189−2524 and Mrk 1014; Dasyra et al. 2011). The high-velocity [C II] emission may hence originate from NLR gas that is sufficiently shielded to be only singly ionized.

Alternatively, and more likely, the high-velocity [C II] emission originates in an outflow, as previously suggested to explain the high-velocity wings in the [C II] profile of Mrk 231 (Fischer et al. 2010) and the high-redshift quasar SDSS J114816.64+525150.3 (Maiolino et al. 2012). Following Hailey-Dunsheath et al. (2010) and Maiolino et al. (2012; their Equations (1)), we use the [C II] line luminosities of the broad component to infer a *lower* limit on the total atomic mass in the outflow. We find values ranging from 2×10^8 $M_{\odot}$ to 4.5×10^8 $M_{\odot}$ (IRAS 20100−4156), which is of the same order as the molecular gas mass seen in the outflow in Mrk 231 (5.8×10^8 $M_{\odot}$) using CO(1–0) (Feruglio et al. 2010).

5. DISCUSSION AND CONCLUSIONS

We have analyzed the *Herschel*-PACS spectra of the two lowest ground-state transitions of OH and ^{18}OH in a sample of 24 ULIRGs. The OH119 and OH79 doublets reveal that P-Cygni type profiles, and thus molecular outflows, are common among late-stage mergers. Smaller subsets of sources in our sample either show pure absorption or pure emission profiles. While these do not necessarily imply outflows, plausible outflow geometries exist that are consistent with their observed line profiles. These geometries require the outflows to be highly obscured (to suppress the emission component) or highly non-spherical in nature (to explain the pure emission or pure absorption profiles).

The molecular gas velocities probed by our observations span a wide range, with some sources showing highest outflow velocities of no more than 100 km s^{-1} while others show maximum outflow velocities of up to 2000 km s^{-1} in their absorption components. Absorption line studies of neutral gas outflows in ULIRGs (Rupke et al. 2005; Martin 2005) suggest that starbursts drive outflows with highest outflow velocities of 500–700 km s^{-1}. In our ULIRG sample, 15/24 sources show maximum OH outflow velocities exceeding this threshold and 10/24 sources have maximum OH outflow velocities above 1000 km s^{-1}. The large majority of our sample ($\sim$2/3) would hence host AGN-driven molecular outflows, powered by radiation pressure on dust grains (Martin 2005; Murray et al. 2005, 2011).

A correlation of both the maximum OH119 outflow speed and the balnicity (similar to the equivalent width of the blueshifted absorption component; Equation (1)) to the SFR and the bolometric AGN luminosity also identify AGNs as the likely driver of these molecular outflows. Since the balnicity is a reasonable proxy for the total momentum in the outflow, the AGN luminosity may correlate with the energy in the outflow. These results confirm the findings of Sturm et al. (2011) for a smaller subset of local starburst galaxies and ULIRGs based on modeling of the observed OH119, OH79, and OH65 doublets.

Correlations with two other parameters, the 9.8 μm silicate strength and the equivalent width of the 6.2 μm PAH emission feature (Figure 9), suggest that the maximum outflow speed is generally higher among moderately to deeply embedded ULIRGs than among ULIRGs with a starburst or an AGN-like mid-IR spectral appearance. This fact would suggest that the most powerful molecular outflows are associated with the early stages of AGN feedback, when the AGN is still deeply embedded. Two deeply obscured ULIRGs in our sample, IRAS 00397−1312 and 11095−0238, appear to be at odds with this interpretation. Neither source shows a P-Cygni type high-velocity OH gas outflow in its spectrum. Instead, both show relatively narrow emission profiles. Both are also extreme outliers in a plot of OH119 equivalent width as a function of silicate obscuration (Figure 5) since they show OH119 purely in emission. As proposed in Section 4.3, this spectral appearance may merely be an orientation effect resulting from the outflow being concentrated in a direction close to the plane of the sky. IRAS 00397−1312 and 11095−0238 may thus host similarly strong molecular outflows as the other deeply obscured sources on the upper branch of the fork diagram (Figure 9). Furthermore, like the other sources on that branch, they may be evolving downward toward the AGN locus (quadrant 1A in Figure 9) as the molecular outflow continues to disrupt and dismantle the obscuring cocoon and expose more of the hot continuum associated with the AGN torus. At the implied high mass loss rates of hundreds to thousands of solar masses per year, as found by the SHINING team (Sturm et al. 2011), the timescale for depletion of the molecular gas reservoir and transition to the AGN locus would range between 10^6 and 10^8 yr. This result would make this downward evolution in the fork diagram a quick transition with relatively few sources caught in mid-transit.

We have furthermore compared the kinematic properties of the mid- and far-IR fine-structure *emission* lines to the kinematic properties of the OH119 *absorption* components. Such a comparison is not straightforward, as the OH119 absorption component probes the velocity field in the line of sight to the far-IR nucleus and the emission lines trace gas all around the source. Comparison of the kinematic information gained from emission and absorption tracers may hence be subject to numerous biases (see, e.g., Westmoquette et al. 2012). The emission lines are density weighted, while the OH119 doublet will be optically thick at most velocities and may not cover the entire far-IR continuum source. With these important

caveats in mind, it may not be surprising that we find no correlation between the kinematic properties of the molecular and ionized gas on a source-by-source basis. And there may not be one, if the different gas phases in ULIRG winds are not strongly coupled (Rupke & Veilleux 2011). Only when the maximum outflow velocities of the OH and ionized neon gas are plotted together as a function of AGN luminosity do the data suggest the existence of a maximum attainable outflow velocity for these species; in some sources the ionized neon gas reaches this highest attainable velocity for a given AGN luminosity, while in other sources it is the molecular gas that reaches these levels. Whether or not this result is significant may be tested by including neon and OH line profile measurements for other ULIRGs observed by *Spitzer*-IRS and *Herschel*-PACS as part of other programs. The latter results are, however, not yet published. Further observations and further analysis will also have to show whether there is a kinematic connection between the decelerating ionized gas outflows, as implied by the mid-IR neon line observations (Spoon & Holt 2009), and the molecular gas outflows as traced by OH.

Finally, four of our sources show high-velocity wings in their [C II] fine-structure line profiles, which can be fit with Gaussian profiles with FWHMs ranging from 800 to 1150 km s^{-1}. If these [C II] pedestals are interpreted as outflow signatures, they imply maximum outflow velocities up to 1000 km s^{-1} and neutral gas outflow masses of at least 2–4.5 $\times$ 10^8 $M_\odot$. Given the lack of reasonable spatial constraints on both the [C II] emitting and the OH absorbing and emitting envelopes, we cannot infer mass outflow rates.

The authors thank the anonymous referee for constructive comments that led to an improvement of this paper. We are grateful to the SHINING team for their collegiality and for providing us with the OH119 line profile of Mrk 231. We further thank Jackie Fischer, Henny Lamers, Thomas Nikola, and Gordon Stacey for discussions, and Dan Weedman and Sylvain Veilleux for sharing OH line scans prior to their publication. V.L. is supported by a CEA/Marie Curie Eurotalents fellowship. E.G.-A. is a Research Associate at the Harvard-Smithsonian Center for Astrophysics, and thanks the Spanish Ministerio de Economía y Competitividad for support under projects AYA2010-21697-C05-0 and FIS2012-39162-C06-01. J.A. acknowledges support from the Science and Technology Foundation (FCT, Portugal) through the research grants PTDC/CTE-AST/105287/2008, PEst-OE/FIS/UI2751/2011 and PTDC/FIS-AST/2194/2012. M.E. thanks ASTROMADRID for support through grant S2009ESP-1496, from Spanish MINECO: AYA2009-07304 and from ASTROMOL: CSD2009-00038. *Herschel* is an ESA space observatory with science instruments provided by European-led Principal Investigator consortia and with important participation from NASA. Support for this work was provided by NASA through an award issued by JPL/Caltech.

Facility: Herschel (PACS)

REFERENCES

Aalto, S., Garcia-Burillo, S., Muller, S., et al. 2012, A&A, 537, 44
Baan, W. A. 1985, Natur, 315, 26
Baan, W. A., Haschick, A. D., & Henkel, C. 1989, ApJ, 346, 680
Benson, A. J., Bower, R. G., Frenk, C. S., et al. 2003, ApJ, 599, 38
Bradford, C. M., Stacey, G. J., Fischer, J., et al. 1999, in The Universe as Seen by ISO, ed. P. Cox & M. F. Kessler (Paris: ESA-SP 427), 861
Choi, E., Ostriker, J. P., Naab, T., & Johansson, P. H. 2012, ApJ, 754, 125
Chung, A., Yun, M. S., Naraynan, G., Heyer, M., & Erickson, N. R. 2011, ApJL, 732, L15
Croton, D. J., Springel, V., White, S. D. M., et al. 2006, MNRAS, 365, 11
Dasyra, K., Ho, L. C., Netzer, H., et al. 2011, ApJ, 740, 94
Debuhr, J., Quataert, E., & Ma, C.-P. 2012, MNRAS, 420, 2221
Di Matteo, T., Springel, V., & Hernquist, L. 2005, Natur, 433, 604
Farrah, D., Bernard-Salas, J., Spoon, H. W. W., et al. 2007, ApJ, 667, 149
Farrah, D., Lebouteiller, V., Spoon, H., et al. 2013, ApJ, accepted (arXiv:1308.4165)
Farrah, D., Urrutia, T., Lacy, M., et al. 2012, ApJ, 745, 178
Feruglio, C., Maiolino, R., Piconcelli, E., et al. 2010, A&A, 518, L155
Fischer, J., Luhman, M. L., Satyapal, S., et al. 1999, Ap&SS, 266, 91
Fischer, J., Sturm, E., Gonzlez-Alfonso, E., et al. 2010, A&A, 518, L41
González-Alfonso, E., Cernicharo, J., van Dishoeck, E. F., Wright, C. M., & Heras, A. 1998, ApJL, 502, L169
González-Alfonso, E., Fischer, J., Graci-Carpio, J., et al. 2012, A&A, 541, 4
González-Alfonso, E., Fischer, J., García-Carpio, J., et al. 2013, A&A, submitted
González-Alfonso, E., Fischer, J., Isaak, K., et al. 2010, A&A, 518, 43
González-Alfonso, E., Smith, H. A., Ashby, M. L. N., et al. 2008, ApJ, 675, 303
González-Alfonso, E., Smith, H. A., Fischer, J., & Cernicharo, J. 2004, ApJ, 613, 247
Hailey-Dunsheath, S., Nikola, T., Stacey, G. J., et al. 2010, ApJL, 714, L162
Harrison, C. M., Alexander, D. M., Mullaney, J. R., et al. 2012, ApJL, 760, L15
Henkel, C., & Wilson, T. L. 1990, A&A, 229, 431
Holt, J., Tadhunter, C., & Morganti, R. 2003, MNRAS, 342, 227
Hopkins, P. F., & Elvis, M. 2010, MNRAS, 401, 7
Kegel, W. H., Hertenstein, T., & Quirrenbach, A. 1999, A&A, 351, 472
Lamers, H. J. G. L. M., & Cassinelli, J. P. 1999, Introduction to Stellar Winds (Cambridge: Cambridge Univ. Press)
Lebouteiller, V., Cormier, D., Madden, S. C., et al. 2012, A&A, 548, 91
Maiolino, R., Gallerani, S., Neri, R., et al. 2012, MNRAS, 425, L66
Martin, C. 2005, ApJ, 621, 227
Moe, M., Arav, N., Bautista, M. A., & Korista, K. T. 2009, ApJ, 706, 525
Murray, N., Ménard, B., & Thompson, T. A. 2011, ApJ, 735, 66
Murray, N., Quataert, E., & Thompson, T. A. 2005, ApJ, 618, 569
Ott, T. 2010, in ASP Conf. Ser. 434, Astronomical Data Analysis Software and Systems XIX, ed. Y. Mizumoto, K.-I. Morita, & M. Ohishi (San Francisco, CA: ASP), 139
Page, M. J., Symeonidis, M., Vieira, J. D., et al. 2012, Natur, 485, 213
Planck Collaboration 2013, A&A, submitted (arXiv:1303.5076v1)
Poglitsch, A., Herrmann, F., Genzel, R., et al. 1996, ApJL, 462, L43
Rupke, D. S., & Veilleux, S. 2011, ApJL, 729, L27
Rupke, D. S., Veilleux, S., & Sanders, D. B. 2005, ApJ, 632, 751
Sakamoto, K., Aalto, S., Wilner, D. J., et al. 2009, ApJL, 700, L104
Saunders, W., Sutherland, W. J., Maddox, S. J., et al. 2000, MNRAS, 317, 55
Sargsyan, L., Lebouteiller, V., Weedman, D., et al. 2012, ApJ, 755, 171
Skinner, C. J., Smith, H. A., Sturm, E., et al. 1997, Natur, 386, 472
Smith, H. A., González-Alfonso, E., Fischer, J., et al. 2004, in ASP Conf. Ser. 320, The Neutral ISM in Starburst Galaxies, ed. S. Aalto, S. Huttemeister, & A. Pedlar (San Francisco, CA: ASP), 49
Somerville, R. S., Hopkins, P. F., Cox, T. J., Robertson, B. E., & Hernquist, L. 2008, MNRAS, 391, 481
Somerville, R. S., Primack, J. R., & Faber, S. M. 2001, MNRAS, 320, 504
Spinoglio, L., Malkan, M. A., Smith, H. A., González-Alfonso, E., & Fischer, J. 2005, ApJ, 623, 123
Spoon, H. W. W., Armus, L., Marshall, J. A., et al. 2009, ApJ, 693, 1223
Spoon, H. W. W., & Holt, J. 2009, ApJ, 703, 270
Spoon, H. W. W., Marshall, J. A., Houck, J. R., et al. 2007, ApJL, 654, L49
Storey, J. W. V., Watson, D. M., Townes, C. H., Haller, E. E., & Hansen, W. L. 1981, ApJ, 247, 136
Sturm, E., Gonzlez-Alfonso, E., Veilleux, S., et al. 2011, ApJL, 733, L16
Sylvester, R. J., Barlow, M. J., Nguyen, Q.-R., et al. 1997, MNRAS, 291, L42
Veilleux, S., Rupke, D. S. N., Kim, D.-C., et al. 2009, ApJS, 182, 628
Walter, F., Weiss, A., & Scoville, N. 2002, ApJL, 580, L21
Westmoquette, M. S., Clements, D. L., Bendo, G. J., & Khan, S. A. 2012, MNRAS, 424, 416
Weymann, R. J., Morris, S. L., Foltz, C. B., & Hewett, P. C. 1991, ApJ, 373, 23